8 Patterns and pathways in nanoparticle self-organization

8.1 Introduction 214
8.2 Self-assembled and self-organized nanoparticle arrays 215
8.3 Pathways for charge transport in nanoparticle assemblies 237
8.4 Conclusion 245
Acknowledgments 245
References 245

MO Blunt, A. Stannard, E. Pauliac-Vaujour, CP Martin, Ioan Vancea, Milovan Šuvakov, Uwe Thiele, Bosiljka Tadić, and P. Moriarty

8.1 Introduction

The assembly of 2D and 3D "supracrystals" from colloidal nanoparticles is a well-established and, in some respects, maturing subfield of twenty-first century nanoscience. Nevertheless, there remain many unresolved questions with regard to the control of the assembly process and, in particular, the degree to which the dynamics of solvent dewetting can be coerced to produce self-organized structures with predictable and tunable morphologies. Key advances in understanding and controlling the self-assembly and self-organization of nanoparticles on solid substrates have, however, recently been made and in this chapter we review the work of a number of groups, including our own, who have contributed in this area over the past decade. We focus on the assembly and properties of *2D* nanoparticle arrays. Moreover, we draw a strong distinction between the terms *self-assembly* and *self-organisation* where the former is used to describe a close-to-equilibrium process that produces a nanoparticle array whose correlation length/periodicity is dictated by interparticle interactions; the latter term describes a far-from-equilibrium process involving matter/energy flow and where correlations over distances much greater than the interparticle spacing can develop.

A number of important reviews of nanoparticle synthesis and self-assembly/organization have been published over the past decade by leaders in the field including Pileni *et al.* (2001;2006;2007), Murray *et al.* (2000), Mirkin *et al.* (Storhoff and Mirkin 1999), and Heath *et al.* (Collier *et al.* 1998). Our aim in this chapter is to complement, rather than revisit, the material covered in those reviews and thus we largely focus on relatively recent forms of self-assembly and self-organization that have demonstrated particular potential for the assembly of nanostructured matter, namely biorecognition and solvent-mediated dynamics. Having discussed the key elements of these processes, we then in Section 8.2 move on to describe the mechanisms and pathways

for charge transport in nanoparticle superlattices and, in particular, the relationship between the current–voltage characteristics and the topology of the lattice.

8.2 Self-assembled and self-organized nanoparticle arrays

8.2.1 Self-assembly of nanoparticle superlattices

Self-assembly and self-organization of nanoparticle superlattices can lead to a vast variety of complex micro-, meso-, and macroscopic structures. Indeed, the appearance of emergent properties on large length scales is the basis for new functional nanomaterials, thus shifting the horizons of nanotechnology well beyond the limits of classical crystalline solids. There are numerous examples of structure–function interdependencies in assembled nanosystems. Here, we list only a few:

- Inorganic nanoparticles assembled via reverse micelles have been organized into two- and three-dimensional supracrystals (Pileni 2001; Pileni 2006). It was shown that the collective dynamical effects induced by the regular arrangements of the nanoparticles cause new optical, magnetic and charge-transport properties (Pileni 2006; Pileni 2007), compared to isolated nanoparticles and to the crystalline bulk form of the material;
- Gold nanoparticles may form different three-dimensional structures if they are linked via programable biorecognition between attached compatible parts of DNA strands (Mirkin *et al.* 1996; Winfree *et al.* 1998; Mirkin *et al.* 2000; Nykypanchuk *et al.* 2008; Park *et al.* 2008). In recent experiments (Nykypanchuk *et al.* 2008; Park *et al.* 2008) regular fcc structures were observed;
- Antigen–antibody recognition with complementary molecules attached to nanoparticles in a solvent, often exploited in biosensing applications (Liron *et al.* 2001), can be used to tune nanoparticle aggregation to form particular types of structure;
- Chemical functionalization of gold nanoparticles allows interactions between particles to take place along pre-specified directions (Archer *et al.* 2007). Attaching such nanoparticles to a branched polymer structure produces an assembly with a novel magnetic response. Theoretical investigations (Tadić 2007) of the field-driven magnetization reversal processes on strongly inhomogeneous spin networks suggest entirely different hysteresis-loop properties, compared to the classical memory materials with moving domain walls. In particular, the coercive field increases with topological disorder. Hysteresis curves have been measured for homogeneous nanoparticle arrays (Duruöz *et al.* 1995; Pileni 2006;);
- Arrays of metallic nanoparticles on substrates are examples of systems that conduct current via single-electron charging, a property of crucial importance in nanoelectronics (Ferry *et al.* 1997; Guéron *et al.* 1999).

A striking feature of conducting nanoparticle superlattices is the emergent non-linearity of the current–voltage curve, which, as discussed below, strongly varies with the structure of the array (Parthasarathy *et al.* 2001; Blunt *et al.* 2007). In Section 8.2 we discuss the processes that underpin these non-linear effects.

In the following, we expand on a number of these topics in detail. Starting with a discussion of the control of self-assembly via biorecognition, we subsequently review solvent-mediated self-organization and pattern formation, before, in Section 8.2, discussing the interplay of morphology/topology and charge transport in 2D nanoparticle supracrystals.

8.2.2 Exploiting biorecognition for nanoparticle assembly

A number of methods have been developed for the assembly of nanoparticles ligated with complementary chemical entities (Mirkin 1996; Mirkin 2000; Nykypanchuk *et al.* 2008; Park *et al.* 2008). Consider two types of colloidal particles, A and B, which are ligated by biopolymers, as shown schematically in Fig. 8.1(a), such that the complementary parts of the molecule are attached to different particle types. Some well-known examples are proteins with specific interactions, e.g., in antigen–antibody recognition (Huber 1986), and in complementary DNA strands (Nykypanchuk *et al.* 2008; Park *et al.* 2008), where the strength of bonding is directly related to the number of complementary base pairs. It was demonstrated recently (Nykypanchuk *et al.* 2008; Park *et al.* 2008) that by varying the lengths of the free and the bonding parts of the ligands, different three-dimensional structures of nanoparticles may emerge, including regular bcc-like supracrystals.

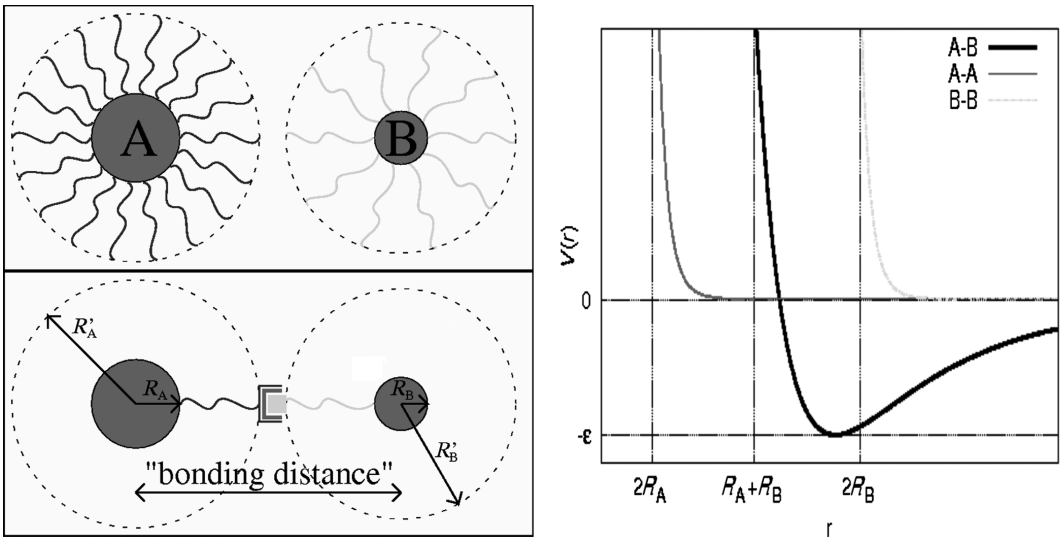

Fig. 8.1 (a) Schematic view of biorecognition bonding between pairs of ligated colloidal particles A and B, and (b) the associated potentials in the binary colloidal mixture with particle radii R_A and R_B (Šuvakov and Tadić 2008a).

The attractive interactions between such particles arise due to both van der Waals interactions and hydrogen bonding and are readily described in the literature by the attractive part of the α-Lennard-Jones potential (Mossa *et al.* 2004; Zaccarelli 2007). The attraction occurs at distances above the "bonding distance", d_{B}, which depends on the particle sizes and the lengths of the attached biopolymers (see Fig. 8.1). At the "bonding distance" particle pair A–B binds together via hydrogen bonding (Nykypanchuk *et al.* 2008) or click-chemistry mechanisms (Brennan *et al.* 2006). At smaller distances $d < d_{\mathrm{B}}$, however, a repulsive interaction starts building up, first as a soft interaction between attached polymer chains, and eventually reaching hard-core repulsion at the "touching distance" $d = R_{\mathrm{A}} + R_{\mathrm{B}}$, as shown in Fig. 8.1(b). We also assume that a large number of polymer chains of the same kind are symmetrically distributed over the particle surface, so that the radial symmetry of the potential is preserved. Hence, in the absence of long-range electrostatic repulsion, the potential for the effective interaction between pairs of particles of different kind is given by:

$$V_{\mathrm{A-B}}(r) = 4\epsilon \left(\frac{\sigma^{12}}{(r - R_{\mathrm{A}} - R_{\mathrm{B}})^{12}} - \frac{\sigma^{6}}{(r - R_{\mathrm{A}} - R_{\mathrm{B}})^{6}} \right), \qquad (8.1)$$

where r denotes the distance between particles, R_{A} and R_{B} are their radii and σ and ϵ are the usual Lennard-Jones parameters. Here, we use $\alpha = 6$, the classical version of the Lennard-Jones potential, given in eqn (8.1), which corresponds to a wide potential well and, thus, allows particle attraction across a wider area. (The potential well becomes increasingly narrow for larger α values (Mossa 2004).) The depth ϵ measures directly the binding strength of the biorecognition pair (Jelesarov 1996). Similarly, the optimal binding distance, corresponding to the potential minimum in Fig. 8.1(b), is related to the parameter σ in view of eqn (8.1). Thus, σ should be appropriately selected for a given particle size. For pairs of equivalent particles, A–A and B–B, we assume repulsive interactions described by the first term in the Lennard-Jones potential:

$$V_{X-X}(r) = 4\epsilon' \frac{\sigma'^{12}}{(r - 2R_X)^{12}}, \qquad (8.2)$$

where R_X stands for R_{A} or R_{B}, and the parameters σ' and ϵ' may, in principle, be different from the those in the A–B interaction.

The kinetics of the binary colloidal mixture can be described by the Langevin equation with the interaction between pairs of nanoparticles given by eqns. (8.1) and (8.2). The Langevin equation of motion for particles in high-viscosity media is given by:

$$\nu_i \dot{\mathbf{r}}_i = -\nabla_{\mathbf{r}_i} \sum_j V_{i-j}(|\mathbf{r}_i - \mathbf{r}_j|) + F_{i,T}, \qquad (8.3)$$

where r_i is the position of ith particle and ν_i represents $\nu_{\mathrm{A}} \equiv 6\pi\eta R_{\mathrm{A}}$ or $\nu_{\mathrm{B}} \equiv 6\pi\eta R_{\mathrm{B}}$, when the ith particle is of the type A or type B, respectively. η is the fluid viscosity coefficient. The stochastic Langevin force $F_{i,T}$ can be seen as originating from the integration over the fluid degrees of freedom. In

the simplest case the fluctuations of the Langevin term are uncorrelated, and described by the moments of a normal distribution with

$$\left\langle F_{i,T}(t)\right\rangle = 0, \tag{8.4}$$

$$\left\langle F_{i,T}(t)F_{j,T}(t')\right\rangle = 6k_{\mathrm{B}}T\nu_i\delta_{i,j}\delta_{t,t'}. \tag{8.5}$$

The standard meaning of these terms, with respect to the Einstein–Smoluchowski relation, is that the diffusion coefficient D_i of the ith particle is given by $D_i = k_{\mathrm{B}}T/\nu_i$, which is generally different for the particles of A and B type, and $k_{\mathrm{B}}T$ is the thermal energy.

We used the fourth-order Runge–Kutta method ($RK4$) to solve the differential eqn (8.3) for the trajectories of colloids of both A and B type. In the simulations the following set of parameters was specified: the size R_{A}, R_{B} and number N_{A}, N_{B} of the particles of type A and B, the respective viscosity (or diffusion) coefficients ν_{A} and ν_{B}, the temperature T, and the parameters of the potential σ and ϵ/k_BT. We start with a random distribution of $N = N_{\mathrm{A}} + N_{\mathrm{B}}$ particles in a box of size $L \times L$ with an infinite potential at the boundaries. At each time step $k \times \Delta t$ the positions of the particles are updated in parallel according to eqn (8.3). A small time step Δt is chosen so that the updated positions of the particles result in a smooth change of the potential. The random Langevin force $F_{i,T}$ is distributed once at each time step according to the symmetric normal distribution with the second moment given by eqn (8.5). Details of the numerical implementation with increased efficiency algorithm are given in (Šuvakov and Tadić 2008).

Note that, due to the ligands attached to each particle, the larger radii marked with R'_{A} and R'_{B} in Fig. 8.1(a), are relevant for the definition of the *coverage* of the box with particles. In the simulations, when two particles bind with compatible chemistry, they stay at the binding distance (which may be larger than the particle radii). A free particle, however, cannot move across the bond. Such constraints on particle motion induce additional effective interactions, making the system condense at non-equilibrium global energy states. These effects depend on the overall particle density and the fraction of the attractive particle pairs compared to the total number, N_{A}/N. In principle, at any finite temperature a bond may break. The process is, however, less probable at low temperatures. Here, we keep $k_{\mathrm{B}}T\epsilon \ll 1$. The system can be additionally "equilibrated" by a sudden increase and subsequent drop of temperature.

For a given ratio of the particle sizes $R_{\mathrm{A}}/R_{\mathrm{B}}$, emergent structures of the nanoparticle aggregates depend on the coverage, $\Phi = A/L^2$, where A is the total area covered by the particles, and on the relative concentrations of two particle types $N_{\mathrm{B}}/N_{\mathrm{A}}$. In Figs. 8.2(a) and (b) we show assemblies obtained with the same total number of particles but with different fractions of the large (A) and small (B) particles. Note that the ratio of the particle sizes $R_{\mathrm{A}}/R_{\mathrm{B}}$ determines the maximum number of small particles that can attach to a single large particle. Local structures with large particles linked via small particles occur, which are joined in an irregular pattern, with voids of different sizes. The walls of such voids are built of large particles in the case of equal con-

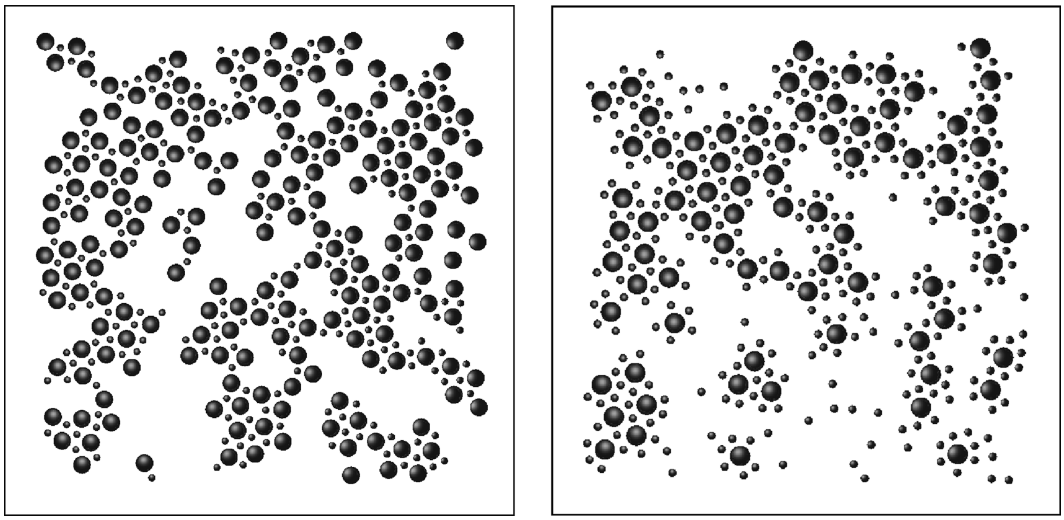

Fig. 8.2 Three-dimensional rendering of simulated nanoparticle assemblies obtained by diffusion and aggregation with biorecognition bonding: two types of particles with size ratio $R_A/R_B = 2.5$ and fixed total number $N_A + N_B$. Concentration ratio, $N_B/N_A =$ (a) 1 and (b) 4.

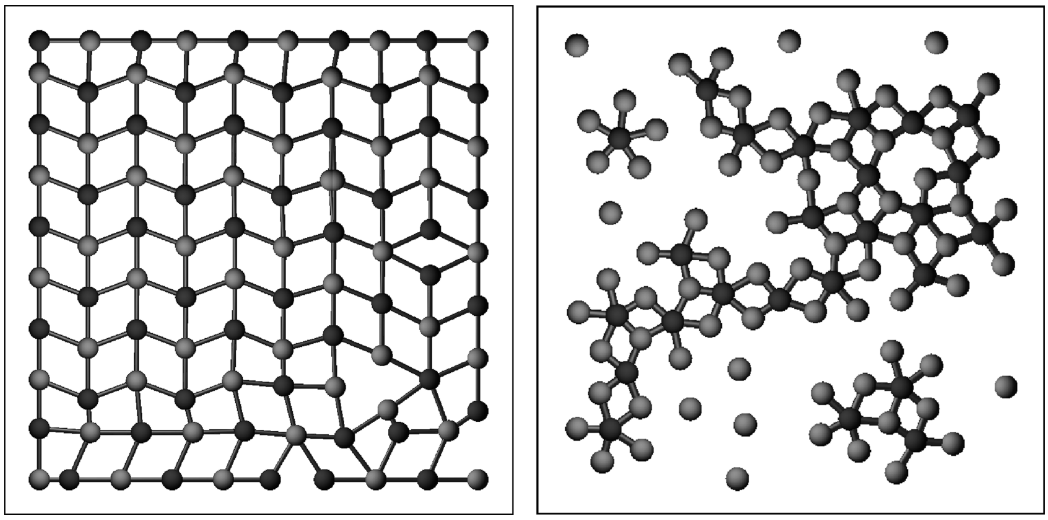

Fig. 8.3 Simulated nanoparticle structures obtained by diffusion and aggregation with biorecognition potentials: Occurrence of periodic structure for equal particle sizes with (a) full coverage with equal concentrations of A and B particles and (b) 50% coverage with concentration ratio 1:3 (Šuvakov and Tadić 2008).

centrations. However, for an abundance of the small particles, as in Fig. 8.2(b), aggregates of different sizes are often isolated by small particles.

An entirely different situation is found when the particle sizes are equal, i.e. the particles differ only by the ligand type. In Fig. 8.3(a) we show the situation corresponding to equal concentrations of particles, when a periodic structure arises. A regular pattern with alternating A-B-A-B particles spans almost the whole system, with only a few topological defects. In the case when one particle type is abundant compared to the other, such structural regularity

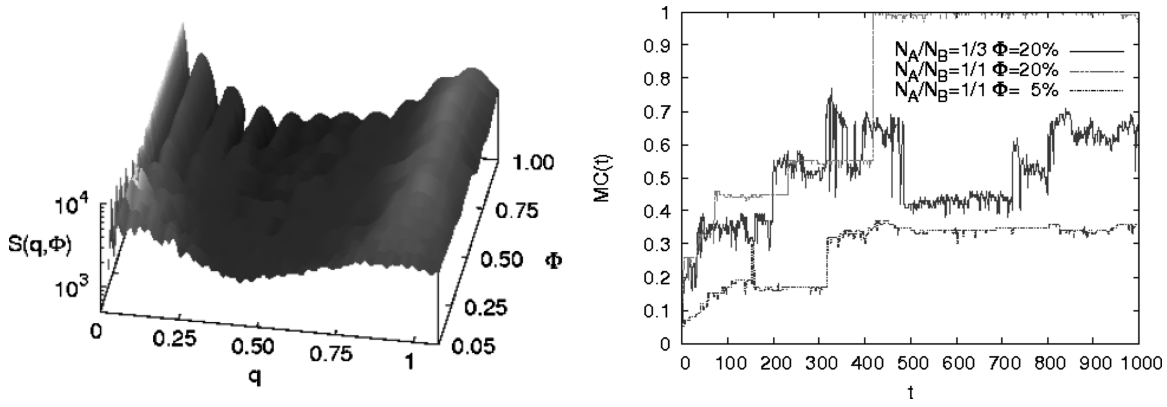

Fig. 8.4 (a) Structure factor $S(q)$ for nanoparticle aggregates obtained by biorecognition bonding for equal size particles and varied coverage Φ. (b) Growth of the largest cluster of connected nanoparticles against time for various values of coverage Φ and concentration ratios N_A/N_B.

remains only at the local level. Large as well as isolated clusters may be found, as in Fig. 8.3(b). In both figures the bonding links between the compatibly ligated nanoparticles are shown.

The regularity of the nanopatterns in our 2-dimensional simulations can be quantitatively measured by computing the structure factor $S(q)$ defined by

$$S(\mathbf{q}) = \left| \sum_{i=1}^{N} \mathrm{e}^{-\mathrm{i}\mathbf{q}\mathbf{r}_i} \right|, \tag{8.6}$$

where r_i are positions of nanoparticles in the 2-dimensional box. In Fig. 8.4 we show $S(q)$ obtained after angular averaging of $S(\mathbf{q})$ and different coverages Φ. The figure shows how the regular structure of nanoparticle assemblies arises, leading to the characteristic oscillatory pattern of the surface $S(q, \Phi)$ (seen in the upper left part), with increased coverage and equal particle size (Šuvakov and Tadić 2008).

The time evolution of the largest cluster, shown in Fig. 8.4(b), reveals the aggregation process in more detail. Depending on the coverage Φ and relative concentrations of the A and B particle types, one can observe that either large clusters join together (marked by large jumps in the upward curves), or small A–B complexes are being attached to a large cluster. In addition, the process is affected by the initial growth of the large cluster, which increasingly slows down cluster diffusion.

8.2.3 Beyond self-assembly: Self-organising nanoparticles

Although liquid-phase self-assembly is an essential component of nanoparticle science, of paramount importance is the intriguing and complex dynamics associated with the transfer of the particles from a colloidal solution to a solid substrate. This involves the evaporative and, in some cases, convective dewetting of the solvent in which the nanoparticles are dissolved. The coupling of the solvent dewetting dynamics with the motion of the nanoparticles leads to a rich parameter space and, thus, a wide variety of complex and correlated

nano- and microstructured patterns result from the drying process. In the following sections we review recent developments in the understanding and control of dewetting-mediated pattern formation in nanoparticle assemblies, focusing in particular on the "archetypal" nanoparticle system: thiol-capped Au particles in organic solvents.

8.2.3.1 *Drying-mediated pattern formation*

Figure 8.5 shows a representative subset of self-organized patterns formed by thiol-passivated Au nanoparticles (∼2 nm diameter) via dewetting of a droplet of colloidal solution on native oxide-terminated Si(111) substrates, taken from the Nottingham group's work on this system. The patterns span a range of morphologies observed not only for Au nanoparticles but a considerable number of other colloidal particle types (including Ag, Co, ferrite, and CdS): isolated droplets, dendritic aggregates, branching and fingering structures, labyrinthine assemblies, cellular networks (on a number of different scales), and isolated rings. While the precise formation mechanisms are in some cases not fully understood, much of the key physics driving the self-organisation process has been elucidated by a number of groups.

Key insights into the physics of the self-organization of colloidal nanoparticles have arisen from the work of Ge and Brus (2000) and Rabani *et al.* (2003). Ge and Brus (2000) proposed that self-organization of colloidal nanoparti-

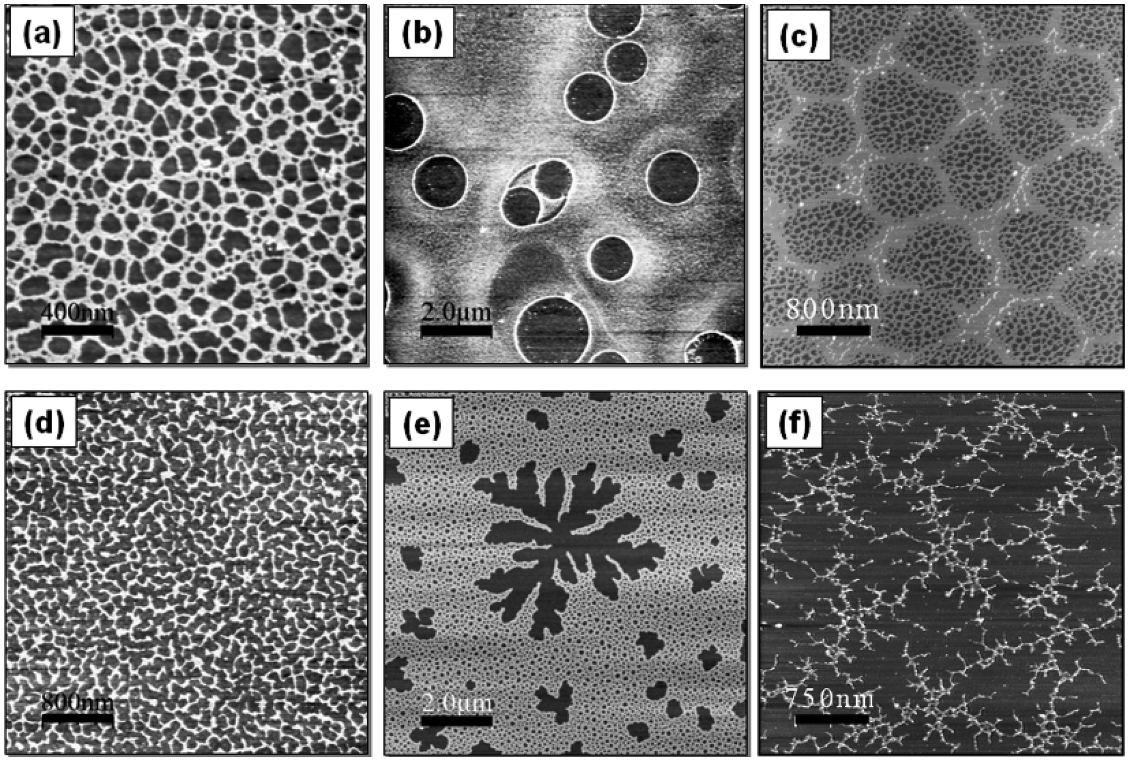

Fig. 8.5 A selection of tapping-mode atomic force microscope (AFM) images of the patterns formed by thiol-passivated Au nanoparticles deposited from an organic solvent onto silicon substrates. The scale bars in the images are: (a) 400 nm, (b) 2 μm, (c) 800 nm, (d) 800 nm, (e) 2 μm, (f) 750 nm.

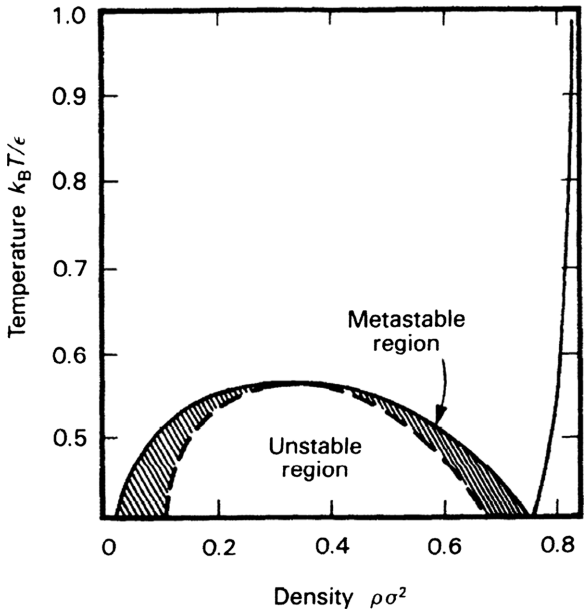

Fig. 8.6 Temperature–density phase diagram of a 2D Lennard-Jones system. The solid line represents the binodal, while the dashed line is the spinodal that separates the metastable (nucleation-and-growth) region from the unstable region. A reduced temperature quench through the critical temperature (0.55 in units of $\frac{k_B T}{\epsilon}$, where ϵ is the interparticle interaction energy) into the unstable region of the phase diagram leads to spinodal decomposition. Reprinted with permission from Koch *et al.* (1983) ©1983 American Physical Society.

cles occured through fluid–fluid spinodal phase separation of a 2D system of particles interacting via a Lennard-Jones-type potential. Figure 8.6 is the universal 2D phase diagram (taken from Koch *et al.* (1983)) around which Ge and Brus based their arguments. Perhaps the most important point with regard to colloidal nanoparticle systems is that evaporation of the solvent is equivalent to a reduced-temperature quench, driving the system from the gas–liquid coexistence region (i.e. the upper region of Fig. 8.6) to phase separation, either in the unstable region of the phase diagram (spinodal decomposition) or in the metastable (nucleation and growth) regime. The critical temperature, in units of $k_B T/\epsilon$ is 0.55, at a coverage of 0.325 monolayer (ML). Removal of the solvent results in less effective screening of the van der Waals interactions between the nanoparticles, driving the phase transition, and producing intricate, spatially correlated patterns of nanoparticles, highly reminiscent of those observed in other systems that phase separate via a spinodal process (binary fluids, polymer blends) – see, for example, Fig. 8.5(d).

Ge and Brus' model captured essential elements of the self-organization of colloidal nanoparticles but, as pointed out by Rabani *et al.* (2003), it neglected the role of solvent fluctuations. Rabani *et al.* put forward an important Monte Carlo model of colloidal nanoparticle (increasingly called "nanofluid") systems that took into account the dynamics of solvent evaporation. In their lattice gas model, the 2D cells are of the size of the liquid coherence length. A dynamic variable ℓ_i, representing fluid density at the ith cell may take two states $\ell_i = 1, 0$, corresponding to the presence or the absence of the liquid. Nanoparticles occupy a given fraction of cells with a density $n_i = 1$ if the nanoparticle occupies the cell i excluding the fluid at that cell, and $n_i = 0$, otherwise. Generally, a single nanoparticle occupies several cells. Typically, in

the simulations the linear size of a nanoparticle is taken to be three times the liquid cell size (Rabani *et al.* 2003; Martin *et al.* 2004).

Attractive interactions occur between pairs of nanoparticles (interaction strengths ϵ_n), liquid–liquid (ϵ_ℓ) and nanoparticle–liquid ($\epsilon_{n\ell}$) according to the Hamiltonian

$$\mathcal{H} = -\epsilon_\ell \sum_{<ij>} \ell_i \ell_j - \epsilon_n \sum_{<ij>} n_i n_j - \epsilon_{n\ell} \sum_{<ij>} n_i \ell_j - \mu \sum_i \ell_i, \qquad (8.7)$$

where $< ij >$ indicates interaction pairs (either nearest neighbors (Rabani *et al.* 2003) or next-nearest neighbors (Martin *et al.* 2004; Yosef and Rabani 2006; Martin *et al.* 2007). The chemical potential μ and the temperature T of the heat bath regulate the equilibrium liquid–vapor concentration.

The kinetics of the model comprise two processes: nanoparticle diffusion and liquid evaporation/condensation. The particle mobility rate (MR) is an important control parameter and determines the relative frequency of events due to these processes. A key element of the model is that nanoparticles can diffuse only in the presence of solvent in cells neighboring the particle. The Monte Carlo dynamics for each of the two processes is performed with the acceptance probability:

$$p_{\text{accept}} = \min(1, \exp[-\Delta H_\kappa / k_B T]), \qquad (8.8)$$

where ΔH_{evap} and ΔH_{diff} are the changes in the total energy associated with the attempted process, computed from the Hamiltonian (7). (Modifications to the Hamiltonian have been recently introduced (Martin *et al.* 2007; Pauliac-Vaujour *et al.* 2008) for reasons to be discussed below.) Figure 8.7 shows a region of the "phase space" for the Rabani model where some of the primary types of nanoparticle assembly observed experimentally–networks, worm-like domains and labyrinths, and droplets–are reproduced.

8.2.4 Regimes of organization: Near-to- and far-from-equilibrium

An impressive aspect of the Rabani *et al.* (2003) model is that it accurately reproduces patterns formed in both the metastable (nucleation-and-growth) and unstable (spinodal) regions of the nanoparticle–solvent phase diagram. Rabani *et al.* refer to these as the heterogeneous and homogeneous limits of solvent evaporation, respectively. Experimentally, these regimes can be accessed via control of solvent volatility–higher vapor pressure solvents drives the system towards the spinodal limit of homogeneous solvent evaporation, whereas slower solvent evaporation moves the system into the heterogeneous limit of solvent evaporation. It is also possible to move between these limits simply by controlling solvent-evaporation time. This has the benefit that a variety of nanoparticle patterns, spanning the homogeneous (spinodal) to heterogeneous (metastable) evaporation limits, can be formed on a single sample.

To systematically and controllably vary solvent-evaporation times, we adopted a deposition approach borrowed from previous work on latex spheres (Denkov *et al.* 1992; Gigault *et al.* 2001), where a PTFE (Teflon) ring is

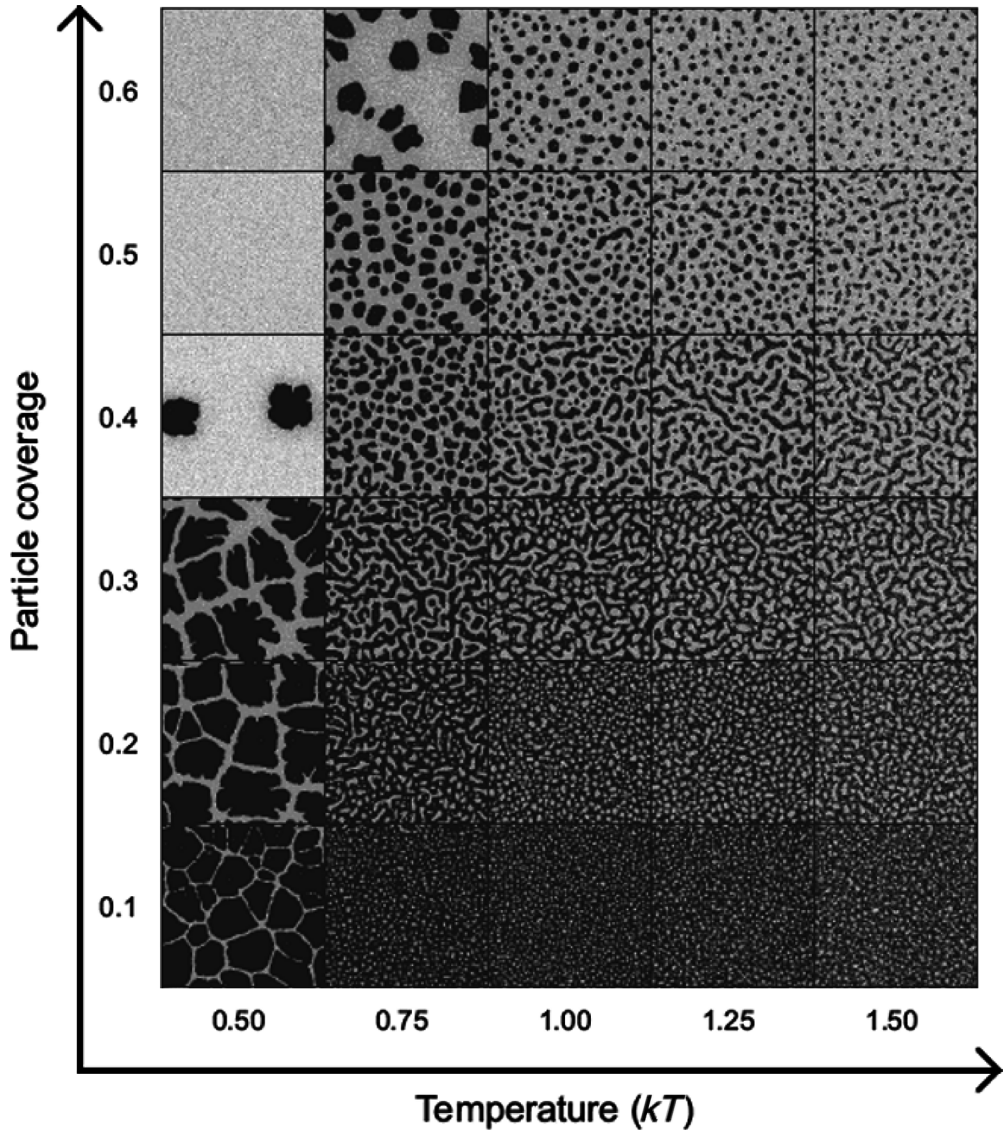

Fig. 8.7 A representative set of nanoparticle assemblies generated using the Rabani *et al.* (2003) Monte Carlo model discussed in the text. A coverage vs. temperature "phase space" is shown where each image is the result of running the simulation for 1000 Monte Carlo steps in a 1024×1024 solvent cell system with $\epsilon_l = 2$, $\epsilon_n = 2\epsilon_l$, $\epsilon_{nl} = 1.5\epsilon_l$, and a mobility ratio of 20.

used to form a meniscus (rather than droplet) geometry for the nanoparticle solution (Pauliac-Vaujour and Moriarty 2007). Figure 8.8 shows a series of atomic force microsope images taken from different areas within the Teflon ring following complete evaporation of the solvent. There is a clear progression from worm-like domains at the center of the ring, arising from rapid ($\sim$ a few tens of seconds) solvent evaporation to a close-packed and relatively void-free monolayer at the edge of the ring, where solvent evaporation can take a few hours. A variety of patterns are observed moving from the center to the

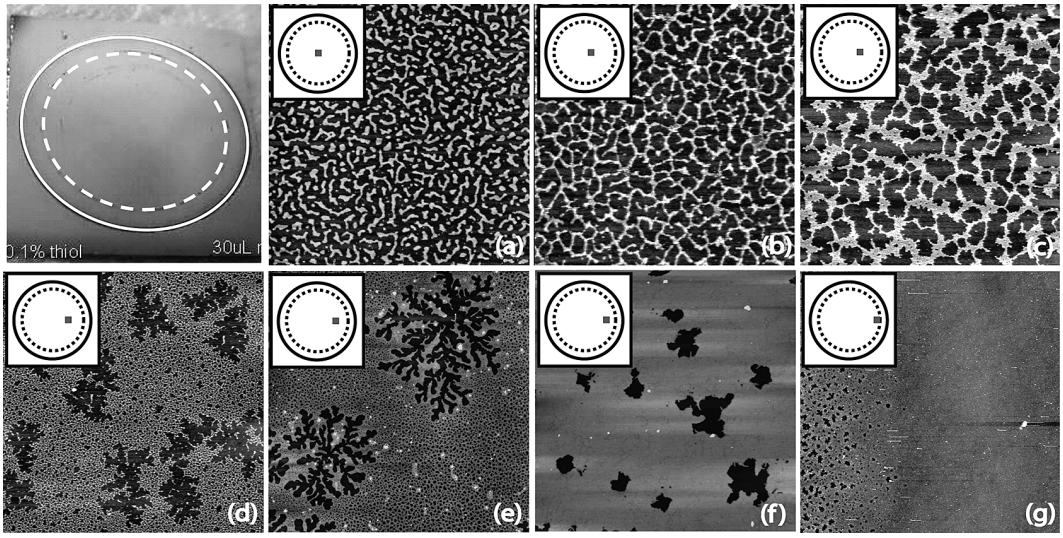

Fig. 8.8 Tapping-mode AFM images of dodecanethiol-passivated Au nanoparticle assemblies on a native-oxide-terminated silicon sample prepared with the meniscus technique described in the text. A photograph of the substrate following evaporation of the Au nanoparticle solution within a teflon ring is shown in the top left. The outer and inner diameters of the ring are shown. The nanoparticle solution used in this case contained 0.1% excess dodecanethiol by volume. In each of (a)–(f), the insert shows schematically the macroscopic region on the sample where the scan is taken. Scans (a)–(c) and (f) are 5 μm × 5 μm in size;(d),(e) and (g) are 20 μm × 20 μm. Reprinted with permission from Pauliac-Vaujour and Moriarty (2007), ©2007 American Chemical Society.

edge of the ring. Importantly, in many cases there is a coexistence of patterns with radically different signature length scales. This is particularly clear in Fig. 8.8(f) where fingered structures reminiscent of those formed in Hele–Shaw cells or during solidification from a melt are surrounded by a high density of small voids forming a nanoparticle network. This observation of pattern formation on distinctly different length scales provides important clues as to the mechanisms of solvent dewetting for nanofluids on solid surfaces and we return to this point below.

In Fig. 8.9, we compare Fig. 8.8(b) with an AFM image taken from the work of Ge and Brus (2000) on CdSe nanoparticle assembly on graphite substrates. Despite the use of entirely different nanoparticle types (Au vs. CdSe) and substrates (SiO_2/Si(111) and graphite), the similarity between the images is striking. In each case, solvent evaporation has been rapid, driving the system into the spinodal regime of phase separation. We also include in Fig. 8.9 a nanoparticle distribution generated by the Monte Carlo code described above. Again, there is extremely good qualitative agreement between the simulated pattern and the experimental data. However, and as we have described at length elsewhere (Martin *et al.* 2004; Martin et al. 2007b), a variety of morphological metrics (Fourier analysis; Voronoi tesselations; Minkowski functionals) also show that the images are *quantitatively* virtually indistinguishable.

Rabani *et al.* (2003) have shown that their Monte Carlo code not only captures the final state of the nanoparticle–solvent system (i.e. in the limit where all, or the vast majority, of solvent has evaporated) but the *dynamics* of the system's approach to equilibrium from a far-from-equilibrium state.

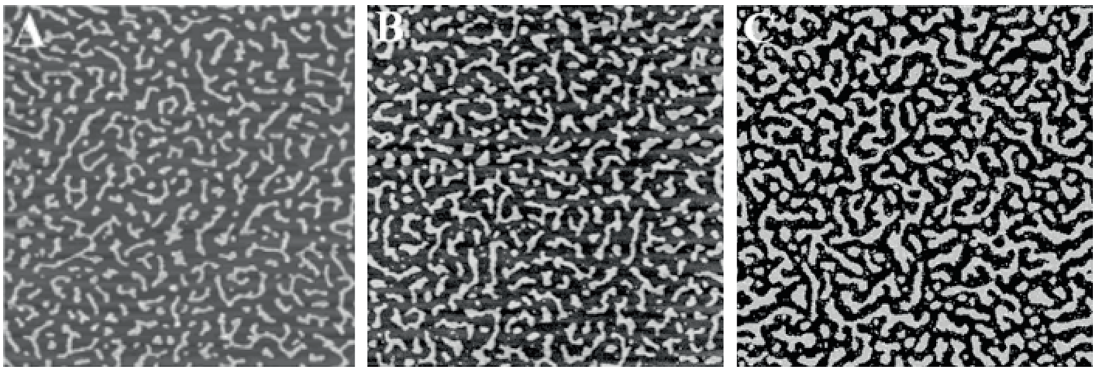

Fig. 8.9 Spinodal nanoparticle assemblies. (A) AFM image of a spinodal pattern formed by CdSe nanoparticles on a highly oriented pyrolytic graphite (HOPG) surface. (Reprinted with permission from Ge and Brus (2000) ©2000 American Chemical Society. The image size is $\sim 3.5 \times 3.5\ \mu m^2$. (B) $5\ \mu m \times 5\ \mu m$ AFM image of dodecanethiol-passivated Au nanoparticles (~ 2 nm diameter) on a native-oxide-terminated Si(111) sample. (C) Nanoparticle distribution generated by Rabani *et al.* Monte Carlo algorithm in the spinodal (homogeneous) limit of solvent evaporation. (See Fig. 8.7).

This evolution towards thermodynamic equilibrium proceeds via self-similar morphologies, is known as *coarsening* or *ripening*, and has been studied, in the context of Ostwald ripening, for example, for a very wide range of systems for over a century. For colloidal nanoparticles (CdSe on graphite), it has been shown that the island distribution scales such that the average size of the domains, r, grows with time, t, as $t^{1/4}$, consistent with a cluster-diffusion-and-coalescence mechanism (Rabani *et al.* 2003). In addition to coarsening via thermally driven nanoparticle diffusion, the AFM probe can be used to *mechanically* drive the transport of nanoparticles and thus locally coarsen a given area. This transport process is akin to a detachment-limited Ostwald ripening process, whereby the tip moves nanoparticles from poorly coordinated sites at the edges of small nanoparticle islands to more highly coordinated, and thus energetically favorable, "bonding" positions at larger islands. The result is again an evolution towards equilibrium via self-similar morphologies but with a scaling exponent of $\frac{1}{2}$, rather than $\frac{1}{4}$, consistent with that expected for detachment-limited Ostwald ripening (Blunt *et al.*, 2007a).

Although, as compared to a close-to-equilibrium process, far-from-equilibrium organization generally gives rise to significantly lower levels of long-range order, in a fascinating recent paper Bigioni *et al.* (2006) have shown that a highly non-equilibrium growth mechanism can produce exceptionally ordered Au nanoparticle superlattices (spanning areas of $\sim 10^8$ particles). The key difference between the arrays produced by Bigioni *et al.* (2006) and the nanoparticle assemblies described thus far (and below) is that organization occurs at the solvent *air*, rather than solvent substrate, interface. By ensuring rapid evaporation, so that the solvent air interface moves more rapidly than the diffusing particles, the nanoparticles are trapped at the interface and, as shown by the real-time video microscopy of Bigioni *et al.*, form 2D islands that eventually coalesce into a large-area, and highly ordered, monolayer. In the final stage of drying, the monolayer is deposited on the substrate. Bigioni

et al.'s work built on earlier important experiments by Narayanan *et al.* (2004) that elucidated, through X-ray scattering measurements, the "interface crushing" effect due to rapid solvent evaporation. With slower evaporation rates, Narayanan *et al.* (2004) found that nanoparticles could diffuse away from the solvent air interface and form 3D supracrystals in the interior of the solvent droplet.

8.2.4.1 *Marangoni convection and network formation*

Although the Rabani *et al.* (2003) Monte Carlo model very successfully predicts and accounts for the observation of a wide range of 2D nanoparticle patterns, the algorithm ignores the contribution of hydrodynamics to the self-organization process (as pointed out by Rabani and coauthors (2003).) Prior to the publication of the Rabani *et al.* (2003) model, the important role that Marangoni convection can play in controlling pattern formation in nanoparticle assemblies had been elucidated by Pileni's group at Université Pierre et Marie Curie, Paris. A Bénard–Marangoni instablity–usually referred to as the Marangoni effect–arises when inhomogeneities in surface/interfacial tension, due to either variations in temperature or solute (e.g. nanoparticle) concentration, are minimized by the flow of fluid across the surface from warmer to cooler regions. The net result is a surface-tension-driven convective flow whose stationary state is a hexagonal or polygonal pattern. This pattern has a characteristic wavelength, λ, given by:

$$\lambda = \frac{2\pi h}{\alpha}, \tag{8.9}$$

where h is the thickness of the liquid film and α is a dimensionless constant related to the Marangoni number, M_a (also dimensionless) as $M_a = 8\alpha^2$. The Marangoni number was put forward by Pearson (1958) in the late 1950s and provides a measure of the balance of the destabilizing effects of the surface tension gradient ($B = \frac{d\gamma}{dT}$) and the suppression of fluctuations due to the thermal diffusivity, κ, and dynamic viscosity, ν, of the liquid:

$$M_a = \frac{B\Delta T h}{\rho \nu \kappa}, \tag{8.10}$$

where ΔT is the temperature gradient across the liquid film and ρ is the liquid density. Far above a critical value of the Marangoni constant, $M_c = 80$, the expression for λ given above (eqn (8.9)) holds and there is thus a well-established relationship between the wavelength of the instability, the temperature gradient across the film, and the variation of surface tension with temperature.

For the volatile solvents used in the nanoparticle experiments described throughout this chapter, the evaporation of the solvent sets up a temperature gradient across the nanofluid film. The more volatile the solvent, the larger the temperature gradient, and thus, from eqn (8.10), the higher the Maranagoni number. Maillard *et al.* (2000) also proposed that higher concentrations of nanoparticles lead to an increase in M_a. Figure 8.10(a), taken from the work of the Pileni group (Maillard *et al.* 2000), shows a TEM image of a network of silver nanoparticles formed via the Marangoni effect. The polygonal nature of

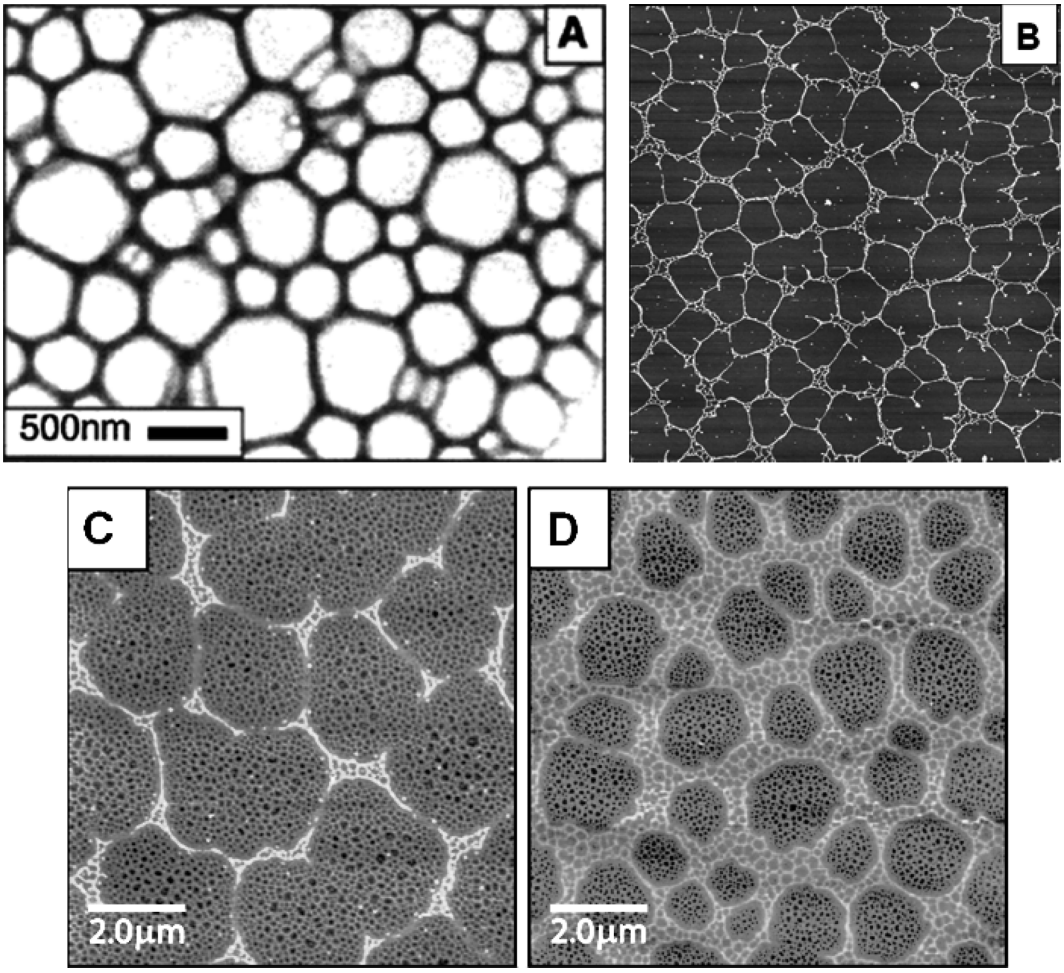

Fig. 8.10 Examples of network formation in nanoparticle self-organization. (A) Transmission electron microscope image of polygonal pattern arising from Marangoni convection in drying Ag nanoparticle solutions. Image reprinted with permission from Maillard *et al.* (2000) ©2000 American Chemical Society. (B) Dual-scale network formation in a submonolayer coverage of pentanethiol-passivated Au nanoparticles (∼2 nm diameter) on a native-oxide-terminated Si(111) sample. Image reprinted with permission from Moriarty, Taylor, and Brust (2002) ©2002 American Physical Society. (C), (D) Multiple-scale network formation in assemblies of dodecanethiol-passivated Au nanoparticle films.

the pattern is clear and the spacing of the cells is broadly in line with estimates of λ based on the experimental parameters. Following the work published by Maillard *et al.* (2000), a detailed study of the formation of honeycomb networks of Au nanoparticles via the Marangoni effect was carried out by Stowell and Korgel (2001). Importantly, they found that a combination of changes in thermal conductivity and B as a function of nanoparticle concentration made "*the most dilute solutions more prone to Marangoni convection*". However, counterbalancing this effect is the necessity to have a sufficiently large number of particles to produce deposits at the edges of the convection cells. Thus, the observation of Marangoni-driven polygonal networks occurs only within a relatively narrow "window" of nanoparticle concentrations.

However, Marangoni convection is not the only mechanism by which nanoparticle networks can be generated. Holes in a dewetting nanofluid open up and grow in either the homogeneous (spinodal) or heterogeneous (nucleation and growth) regimes of solvent evaporation described in the preceding section. For very dilute concentrations of nanofluid solution, rings of nanoparticles can form (see below). With increasing nanoparticle concentration, evaporative dewetting alone—i.e. *without any form of convective fluid motion*—can produce polygonal patterns arising from the collision of expanding holes in the solvent film. Indeed, and as shown in Fig. 8.7, these types of network are readily produced by the Rabani *et al.* Monte Carlo code. Moreover, networks spanning a number of length scales can coexist within the same area on the surface of a sample. Figure 8.10 includes a number of striking images of this effect. In an AFM and statistical crystallography analysis of cellular/polygonal structures formed by nanoparticle assemblies (Moriarty *et al.* 2002) it was proposed that both Maranagoni convection and a spinodal mechanism could give rise to "nested" networks of the type shown in Fig. 8.10.

As described by Martin *et al.* (2004), although a spinodal dewetting/decomposition mechanism is associated with a well-defined preferred length scale that one might not initially expect for networks formed by a nucleation-and-growth process, distinguishing between the morphologies generated by the two types of process is not always straightforward. Although for nucleation-and-growth one would expect the initial dewetting sites to be spatially uncorrelated (i.e. follow a Poisson distribution), the expansion and coalescence of the nucleated holes "washes out" the Poisson distribution, producing a correlation function reminiscent of that for a 2D ensemble of hard discs. That is, there is a reasonably well-defined mean hole separation that appears as a peak in a radially averaged Fourier transform or is evident from Voronoi tesselation and Minkowski functional analyses of AFM images (Martin *et al.* 2004). Similar difficulties in distinguishing spinodal- and nucleation-mediated morphologies are described in the literature on polymer and thin-film dewetting phenomena (see Jacobs *et al.* (1998) and references therein).

8.2.4.2 *Rings and fingering instabilities*

In their studies of the role of the Marangoni effect in driving the self-organization of nanoparticles, Maillard *et al.* (2000) observed the formation of rings of particles whose diameters ranged from a few hundred nm to a few micrometers. Rings of this type had first been reported by Ohara *et al.*, (1997) and a typical example, taken from Ohara *et al.*'s work, is shown in Fig. 8.11(a). Many groups, including our own (see Fig. 8.11(d)), have observed ring formation as a result of drying nanofluids on solid substrates: FePt (Zhou *et al.* 2003), polypyrrole (Jang *et al.* 2004), Ni (Cheng *et al.* 2006), barium hexaferrite (Shafi *et al.* 1999), Au, Cu, Co, ferrite, and CdS (Maillard *et al.* 2000) nanoparticles all form well-defined sub-micrometer or micrometer-scale rings.

Ohara and Gelbart (1998) put forward a general theory to explain the organization of nanoparticles into rings. They argued that ring formation is caused by the nucleation of holes in a nanofluid film due to evaporation (as discussed in previous sections) or disjoining pressure. As a hole expands, nanoparticles

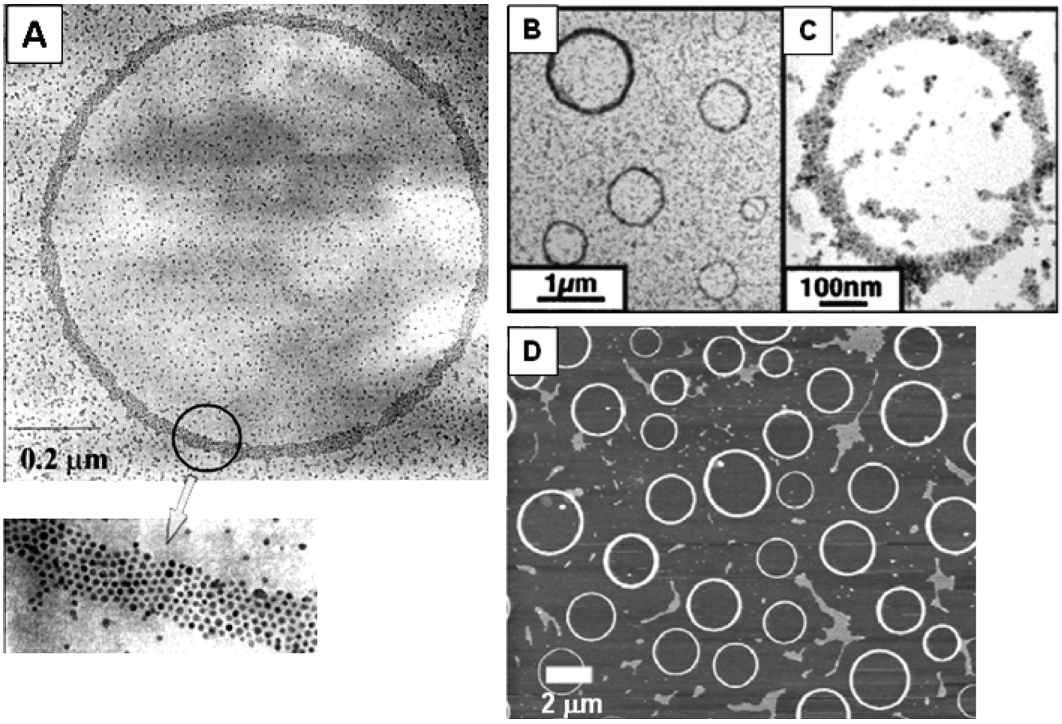

Fig. 8.11 Examples of ring formation in nanoparticle self-organization. (A) TEM image of a ring formed by dodecanethiol-passivated 2.5-nm diameter Ag nanoparticles. Reprinted with permission from Ohara, Heath, and Gelbart (1997) ©1997 American Chemical Society. (B), (C) TEM images of CdS nanoparticle rings. Reprinted with permission from Maillard *et al.* (2000) ©2000 American Chemical Society. (D) AFM image of rings formed by octanethiol-passivated ∼2-nm Au nanoparticles deposited from dichlormethane via spin casting onto a native-oxide-terminated Si(111) surface. The solution contained an excess of 0.1% by volume of octanethiol.

"track" its rim (due to solvation forces). In Ohara and Gelbart's model, the hole stops expanding when a sufficiently high density of nanoparticles has been reached. That is, the ring diameter is fundamentally controlled by the frictional force between the nanoparticles and the substrate. A modified version of the Rabani *et al.* Monte Carlo model described in previous sections, which models a 3D rather than 2D nanofluid, has also been used to study ring formation (Yosef and Rabani 2006). Use of a 3D model enabled the rate of solvent evaporation, rate of hole growth, and rate of hole nucleation to be effectively decoupled. Yosef and Rabani found both similarities and key differences with the theoretical approach put forward by Ohara and Gelbart (1998). In particular, their results indicated that the growth of the ring halts not when a critical nanoparticle density is reached but when the thin solvent layer evaporates. Moreover, Yosef and Rabani found that there was a negligible dependence of ring size on nanoparticle density.

In the course of their simulations of ring formation, Yosef and Rabani observed the generation of well-developed fingering instabilities in certain regions of parameter space, as shown in Fig. 8.12. We have recently focused our experiments on the generation of fingering instabilities (Pauliac-Vaujour *et al.* 2008) and find that the nanoparticle diffusion rate (or the effective

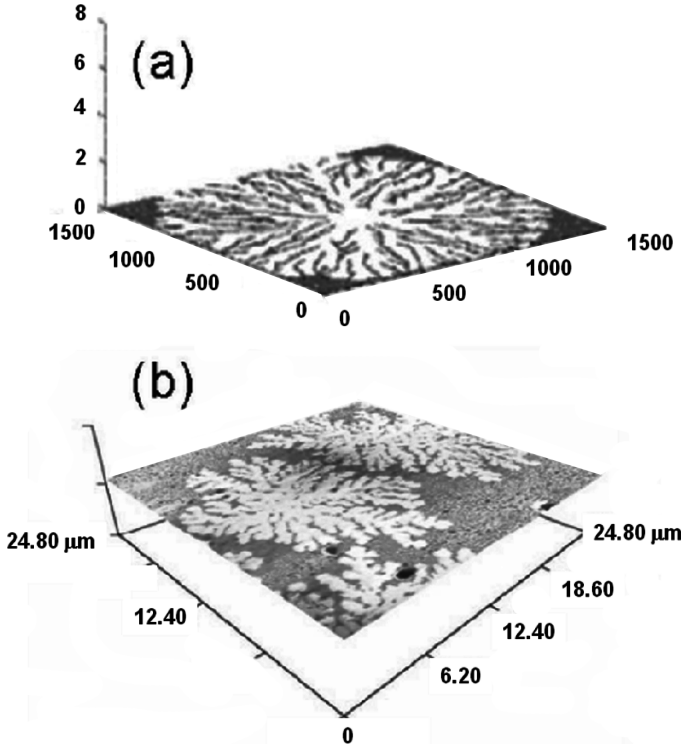

Fig. 8.12 A comparison of fingering structures produced in (a) a 3D Monte Carlo simulation (reprinted with permission from Yosef and Rabani (2006) ©2006 American Chemical Society), and (b) in experiment. AFM image of structure formed in a dewetting nanofluid comprising dodecanethiol-passivated Au nanoparticles (∼2 nm diameter) in toluene with a 0.1% by volume excess of dodecanethiol.

viscosity of the nanoparticle solution) must be tuned appropriately to produce well-developed fingering patterns of the type simulated by Yosef and Rabani. In Fig. 8.12 we show a direct comparison between the patterns generated by Yosef and Rabani and an AFM image taken from the Nottingham group's work on fingering instabilities in colloid Au nanoparticle solutions. Figure 8.13 shows a series of experimental AFM images of self-organized Au nanoparticle monolayers where we have systematically varied the thiol chain length so as to modify the nanoparticle diffusion rate. Addition of a small amount of excess thiol (Figs. 8.13(f)–(j)) increases the viscosity of the nanofluid and dramatically enhances the development of fingered structures.

8.2.4.3 *Combined nucleation-driven and spinodal dewetting*

A striking characteristic of many of the patterns formed by dewetting nanofluids is the presence of self-organization on two or more distinct length scales. Although we touched on this point in the section on network formation above, it is important that we revisit the question of dual-scale (or multiscale) organization via dewetting for two reasons: (i) the organization of matter across a hierarchy of length scales has particular potential in the generation of self-organized materials and devices; and (ii) the presence of multiple length scales in self-organized colloidal nanoparicle arrays provides key insights into the solvent dewetting processes.

The combined effects of nucleation-mediated and spinodal dewetting are responsible for pattern formation on two distinct length scales in the AFM images of fingering structures shown in Fig. 8.13. In Fig. 8.14 we show a

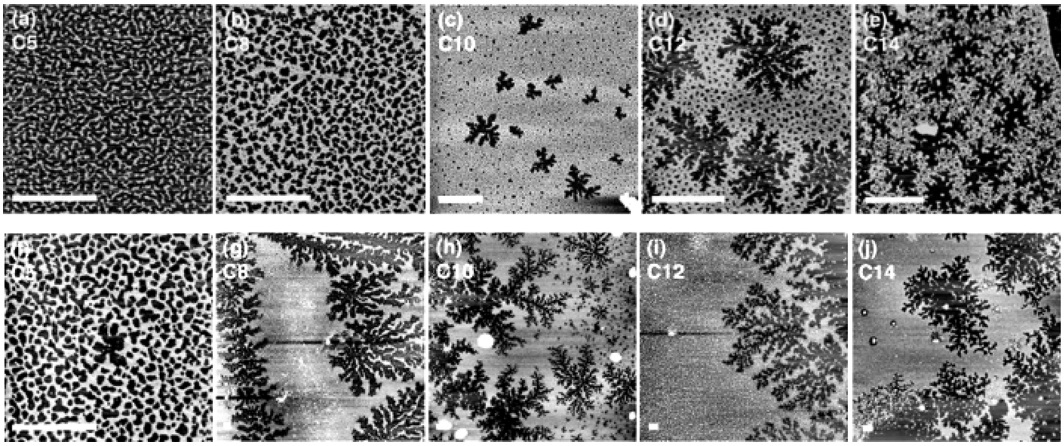

Fig. 8.13 AFM scans of (a,f) C_5-, (b,g) C_8-, (c,h) C_{10}-, (d,i) C_{12}- and (e,j) C_{14}-thiol-passivated gold nanoparticles deposited from toluene onto native-oxide-terminated Si(111). Samples (a–e) were prepared without excess thiol, samples (f–j) with solutions containing 0.1% excess thiol by volume. Figure and caption reproduced from Pauliac-Vaujour *et al.* (2008) with permission ©2008 American Physical Society.

high-resolution image where a high density of holes surrounding the branched structure is clearly visible. Importantly, the small holes have a rather narrow size distribution, suggesting that they appeared within a relatively narrow time window. In order to reproduce "dual-scale" pattern formation of this type, we have modified the Hamiltonian of the Rabani *et al.* (2003) model (eqn (8.11)) so that the chemical-potential term is no longer constant but is a function of solvent coverage, ν:

$$E = -\epsilon_l \sum_{<ij>} l_i l_j - \epsilon_n \sum_{<ij>} n_i n_j - \epsilon_{nl} \sum_{<ij>} n_i l_j - \mu(\nu) \sum_i l_i. \qquad (8.11)$$

An important consequence of mapping the chemical potential onto the solvent coverage in this fashion is that we effectively build in some degree of 3D character to the simulated film of solvent (although the Monte Carlo algorithm is still carried out on a 2D grid). Alternatively, and equivalently, if we consider the solvent coverage as representative of the mean thickness of the solvent film, by introducing a solvent-coverage-dependent chemical potential we introduce a disjoining pressure contribution to the Hamiltonian (Martin *et al.* 2007a; Pauliac-Vaujour *et al.* 2008).

If we now make the chemical potential a step (sigmoidal) function of the solvent coverage (Pauliac-Vaujour *et al.* 2008) we can drive the system from a nucleation regime to a spinodal regime of dewetting (or, in the language of Rabani *et al.* (2003)), from heterogeneous to homogeneous evaporation) at a critical solvent coverage. Figure 8.14 shows a number of frames from a simulation of fingering instabilities in a nanofluid where we have carried out this switch in chemical potential. Initially, a hole at the center of the simulation grid nucleates and grows until the solvent coverage reaches a value that "triggers" rapid spinodal dewetting and to a large extent freezes further development of the fingers.

Returning to the subject of dual-scale networks, it is possible to use the coverage-dependent chemical-potential approach to reproduce a number of

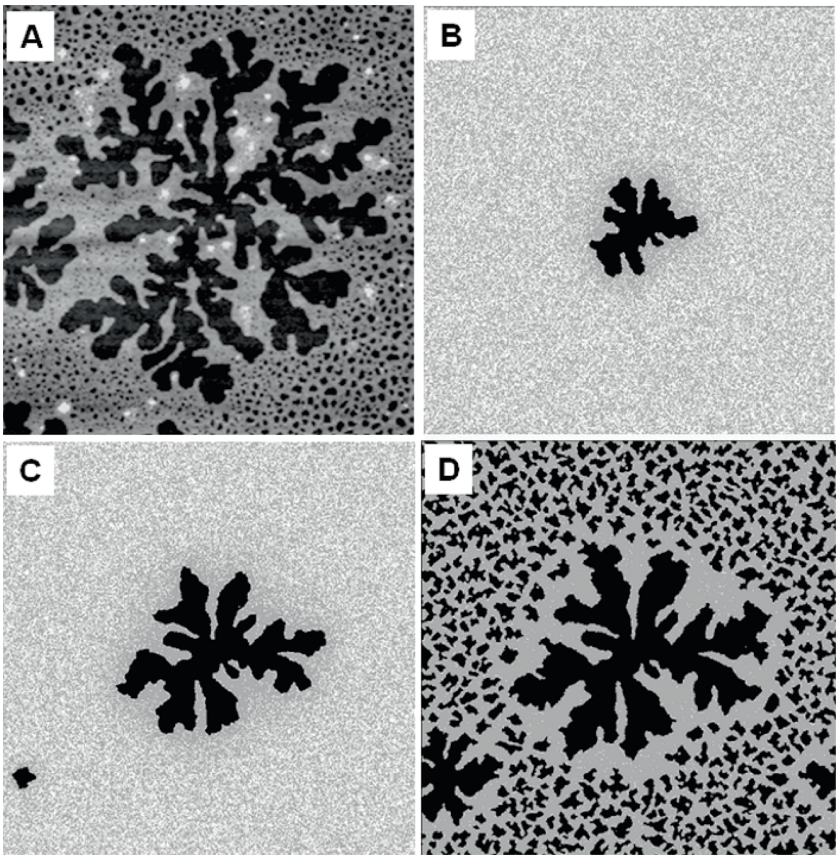

Fig. 8.14 (A) Fingering pattern formed in a submonolayer coverage of dodecanethiol-passivated Au nanoparticles deposited from toluene with an excess of dodecanethiol (0.1% by volume) using the meniscus technique described above. Note the high areal density of holes that surround the fingered structure. (B)–(D) Frames from a Monte Carlo simulation, using the coupled chemical potential–solvent coverage approach described in the text, which show the evolution of a fingered structure and, at late stages of solvent dewetting, the formation of a high areal density of holes due to a spinodal process.

other morphologies observed experimentally. This is shown in Fig. 8.15 for a power-law (rather than sigmoidal) dependence of the chemical potential on solvent coverage. At values of the exponent A between $\sim$0.3 and 4.0, a very clear *bimodal* distribution of cell sizes is present, in good agreement with experiment. Thus, although Marangoni convection coupled with a spinodal dewetting mechanism certainly can give rise to dual-scale networks (Moriarty *et al.* 2002) (as discussed in Section 8.1.4), the simulation results shown in Fig. 8.15 illustrate that the presence of hydrodynamically driven solvent flow is not a pre-requisite for the generation of multiscale networks. A combination of nucleation-driven and spinodal dewetting alone is sufficient. Similar arguments regarding the joint contribution of nucleation- and spinodal-driven mechanisms have been put forward for dewetting of suspensions of macromolecules. The competition of nucleation and spinodal processes has been discussed by Thiele *et al.* (1998) and Thiele (2003) for systems without evaporation.

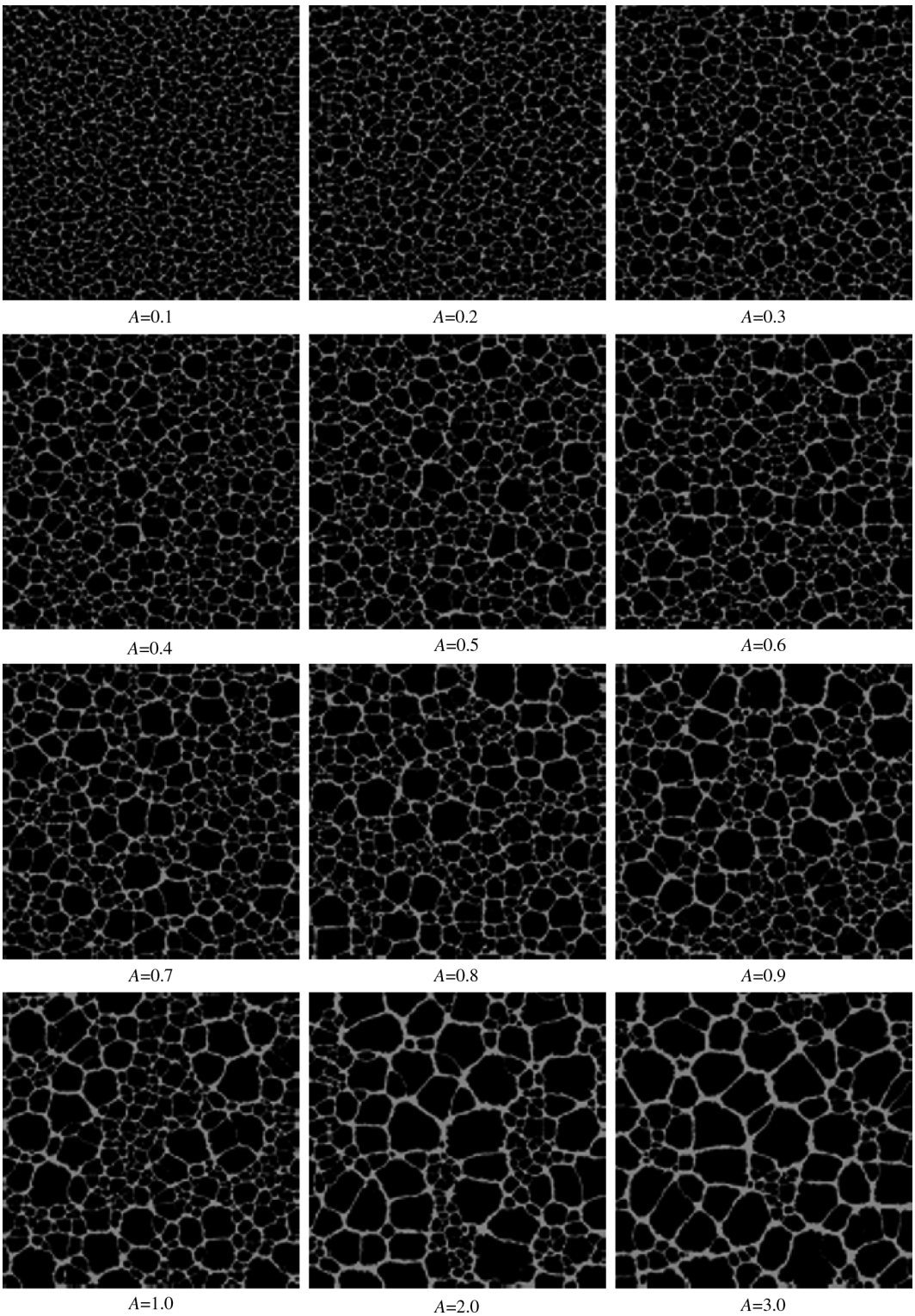

Fig. 8.15 Generation of dual-scale nanoparticle networks via a "dynamic" chemical potential of the form $\mu(\nu) = \mu_0 + (0.1\mu_0 \times \nu^A)$, where ν is the fraction of solvent that has become vapor, and μ_0 is the value of μ (the chemical potential) at the start of the simulation. All images are 2048×2048 lattice sites with $k_B T = \epsilon_l/2$, $\epsilon_n = 2\epsilon_l$, $\mu_0 = -2.25\epsilon_l$, coverage $= 30\%$ and mobility ratio $= 30$. The value of A is given under each image.

8.2.4.4 *Controlling pattern formation via solvent dewetting*

There have been a number of very impressive examples of coercing the solvent dewetting process so as to form highly ordered 1D or quasi-1D structures over very large length scales (up to millimeters square). In particular, elegant control of the motion of the three-phase contact line through the use of a sphere-on-flat geometry (a spherical lens on a silicon wafer) has been demonstrated by Xu *et al.* (2007). They have formed concentric, submicrometer-wide rings of 5.5-nm CdSe/ZnS nanoparticles and, with slightly smaller (4.4 nm) particles, have found that a fingering instability produces "spokes" that propagate transverse to the dewetting front direction. Similar stripe patterns (albeit for somewhat larger particles) have been produced by Huang *et al.* (2005) using a Langmuir–Blodgett approach.

Thus far throughout this chapter we have focused on pattern formation on homogeneous, unpatterned surfaces. An intriguing question, and an issue that has been explored in some depth by the polymer community (see Geoghegan and Kraush 2003 for a review), relates to the influence that a topographically or chemically heterogeneous substrate has on the dewetting process. We have explored this by exploiting a scanning probe technique pioneered by Dagata *et al.* (1991), Lyding *et al.* (Shen *et al.* 1995), and Avouris *et al.* (1997) in the 1990s: local oxidation of hydrogen-passivated silicon surfaces. In our case, a metallized AFM probe is biased with respect to a HF-treated Si(111) sample and used to write patterns of silicon oxide with linewidths down to approximately 20 nm (and feature heights $\sim$2 nm). The HF treatment renders the surface exceptionally hydrophobic, in contrast to the polar oxide regions created by the tip. Thus, the AFM local oxidation procedure produces a topographically and chemically patterned substrate with almost arbitrary control over the topography of the pattern. Some simple patterns are shown in Fig. 8.16.

Our "directed dewetting" experiments were motivated not only by the analogous experiments carried out by the polymer community but by three earlier key papers related to control of spatial nanoparticle distributions via changes in solvent behaviour. Korgel and Fitzmaurice (1998), in a seminal study, showed that the polarity of the solvent directly controlled the thickness of a nanoparticle film deposited from that solvent onto a substrate. The question we initially sought to address was whether *substrate* polarity could be used to have a similar–but locally controllable–effect on nanoparticle organization. The first steps in this direction had been made by researchers at the Nanoscale Physics Laboratory at Birmingham in the late 1990s (Parker *et al.* 1999) who used lithographically patterned resists (at the micrometer scale) to influence the flow of solvent and thus influence nanoparticle distributions. Lu *et al.* (2004) subsequently showed that an anisotropically patterned L-R-dipalmitoyl-phosphati-dycholine (DPPC) film could be used to control solvent dewetting and thus form linear stripes of CdSe or CdSe/ZnS nanocrystals. An important objective of our experiments was to ascertain the extent to which pattern formation in dewetting nanofluids could be controlled at the submicrometer or nanometer length scale via topographic and chemical surface heterogeneities.

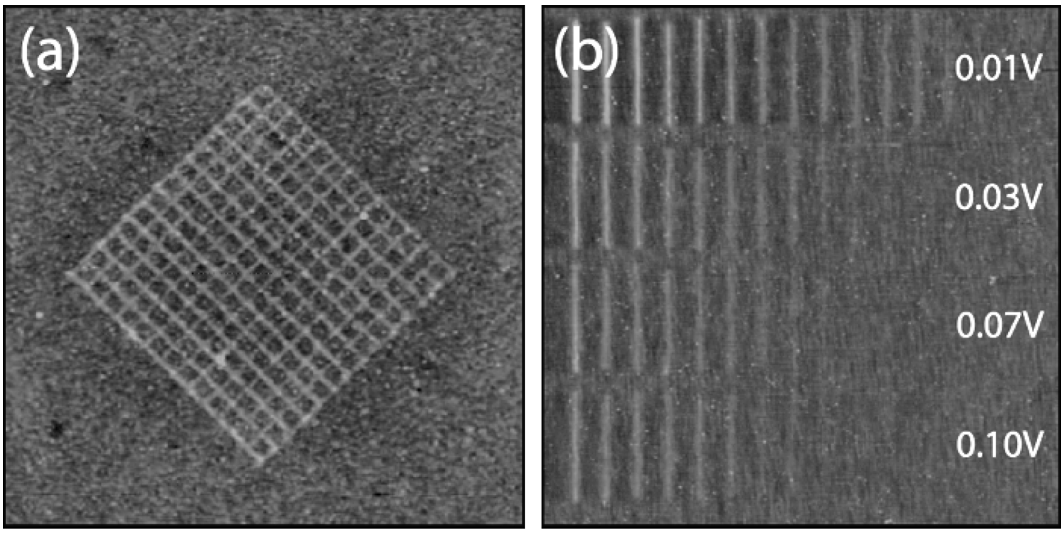

Fig. 8.16 (a) Oxide grid pattern produced on a hydrogen-passivated Si(111) surface using scanning probe oxidation. The grid is 1 μm × 1 μm in area and comprises lines that are ∼2 nm in height and ∼50 nm wide. (b) Effect of tapping-mode voltage set point and tip bias on the width and height of scanning-probe-generated oxide lines on H:Si(111). Set of lines written at set points of 0.01 V, 0.03 V, 0.07 V, and 0.1 V are shown. For each set of lines the tip bias voltage was varied between 10 V and 3V in 0.5 V steps from left to right. The scan speed and relatively humidity were kept constant at 0.5 μm s^{-1} and 70%, respectively.

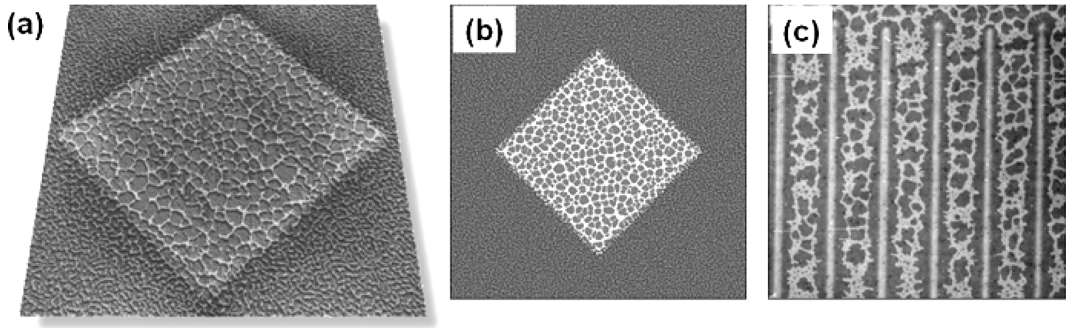

Fig. 8.17 (a) 3D representation of an AFM image showing the effect of an AFM tip-generated oxide square of 4 μm × 4 μm area on the organization of octanethiol-passivated Au nanoparticles on a H:Si(111) surface. (b) Result of a simulation using the original Rabani *et al.* (2003) Hamiltonian with $|\mu|$6% smaller on the simulated oxide region. (Reprinted with permission from Martin *et al.* (2007a) ©2007 American Physical Society.) To reproduce the sharp transition between nucleation-dominated and spinodal-dominated dewetting oberved in the experiment, a 100-nm wide region at the edge of the oxide feature was included over which the chemical potential varies linearly from its value on the H:Si(111) surface to that on the oxide. (c) Narrower oxide features lead to the rupture of the solvent film, producing a region denuded of nanoparticles in the vicinity of the surface heterogeneity.

The degree to which spatial control of pattern formation in dewetting nanofluids can be achieved is best exemplified by Fig. 8.17(a) where the oxide square at the center of the image has clearly dramatically affected the solvent evaporation dynamics. A Monte Carlo simulation using the original Hamiltonian of the Rabani model, but with a reduction of the absolute value of the chemical potential in a square region whose area was chosen to match that formed in the experiment, reproduces the experimental data extremely well (Fig. 8.17). There is a remarkably seamless transition from a wormlike

pattern, characteristic of a spinodal dewetting mechanism, on the hydrophobic H:Si(111) surface, to a network structure arising from nucleation-driven dewetting on the oxide square. What is particularly intriguing about the images shown in Fig. 8.17 is the remarkably sharp switch from one pattern type to another–there is no evidence of a rupture of the solvent film that would give rise to a region denuded of particles close to the edges of the oxide square. To replicate this in the simulations required a linear variation of μ, over an approximate 100 nm length scale, at the edge of the oxide region. Narrower (higher aspect ratio) oxide structures (as in Fig. 8.17(c)), however, exhibit a region free of nanoparticles in their vicinity.

The scanning probe oxidation technique has the advantage that arbitrary oxide patterns can be written with relative ease on a H:Si(111) surface. We are currently pursuing the use of oxide features to induce solvent dewetting in highly localized surface areas and, in particular, exploring the extent to which arrays of oxide sites can be used to direct self-organization of a variety of nanoparticle (and nanorod) types.

8.3 Pathways for charge transport in nanoparticle assemblies

In terms of its electronic and charge-transport properties, a nanoparticle array can be described as a set of coupled Coulomb-blockade devices (Ferry and Goodnick 1997). Coulomb blockade occurs when the charging energy of a metal particle, $e^2/2C$ is significantly larger than the thermal energy, $k_{\mathrm{B}}T$, such that transfer of an electron onto the particle blocks the addition of further electrons until the voltage is increased to offset the charging energy. In a seminal paper in the early 1990s, Middleton and Wingreen (MW) (1993) established and studied a theoretical model of non-linear charge transport in arrays of capacitively coupled metal dots, of sufficiently small capacitance to exhibit single-electron charging (Coulomb blockade) effects, where electrons tunnel from dot to dot. Their key result was that, in the presence of random offset charges (which locally gate the metal particles), the current through the array, above a voltage threshold, V_{T}, exhibits a power-law dependence on voltage:

$$I \sim (V/V_{\mathrm{T}} - 1)^{\zeta}. \tag{8.12}$$

MW highlighted that there is an elegant analogy that can be drawn between charge transport in metal particle arrays of the type they studied and interface growth problems, including, in particular, those involving the Kardar–Parisi–Zhang (1986) (KPZ) model. From the KPZ model MW determined critical exponents for current and correlation lengths in the metal-particle array system, predicting $\zeta = \frac{5}{3}$ for 2D arrays.

Almost a decade later, Parthasarathy *et al.* (2001) carried out a pioneering study of the charge-transport properties of a highly ordered 2D monolayer of thiol-passivated Au nanoparticles (diameter ∼2 nm), reproducing experimentally the $I \sim (V/V_{\mathrm{T}} - 1)^{\zeta}$ dependence predicted by MW but measuring a substantially higher value of the scaling exponent, $\zeta = 2.25 \pm 0.1$. Parthasarathy

et al. (2001) found that topological disorder in nanoparticle arrays (the presence of voids) gives rise to deviations from simple single power-law behavior, where values of ζ varying between $\sim$1 and $>$2.5 could be observed. They argued that bottlenecks in charge transport due to the presence of voids led to the absence of single scaling behavior, a proposal that was confirmed by the subsequent molecular-dynamics simulations of Reichhardt and Olson Reichhardt (2003a, 2003b).

While a number of groups have explored the charge-transport properties of ordered or relatively weakly disordered lattices of nanoparticles (Geigenmuller and Schon 1989; Bakhalov *et al.* 1991; Middleton and Wingreen 1993; Parthasarathy *et al.* 2001; Reichhardt and Olson Reichhardt 2003a, 2003b; Parthasarathy *et al.* 2004; Elteto *et al.* 2005), we have focused on combined experimental and numerical simulation work on topologically complex self-organized assemblies of the type discussed at length in the preceding sections. In the following we discuss how the dewetting-induced complex topology of nanoparticle networks affects the single-electron charging-mediated conduction paths focusing, in particular, on networks of the types shown in Fig. 8.18.

In order to quantify the effects of network structure and topology on conduction, we construct a network (graph) of nanoparticles, by inserting a link between each pair of the nanoparticles that are spaced from one another within a tunnelling radius for the electrons. Thus, each link between the adjacent nanoparticles, which is given by a non-zero element $A_{ij} = 1$ of the respective adjacency matrix, represents a possible junction for tunnelling. The tunnelling radius r, which defines the maximum length of the junction, depends on the physical properties of the nanoparticles. It is clear that the morphology of holes in the evaporated nanoparticle films will affect the network of junctions. Some topological features of these networks that are relevant to the conduction are given in Fig. 8.19a. Specifically, in the inhomogeneous array the number of junctions attached to a nanoparticle varies within a larger range compared to

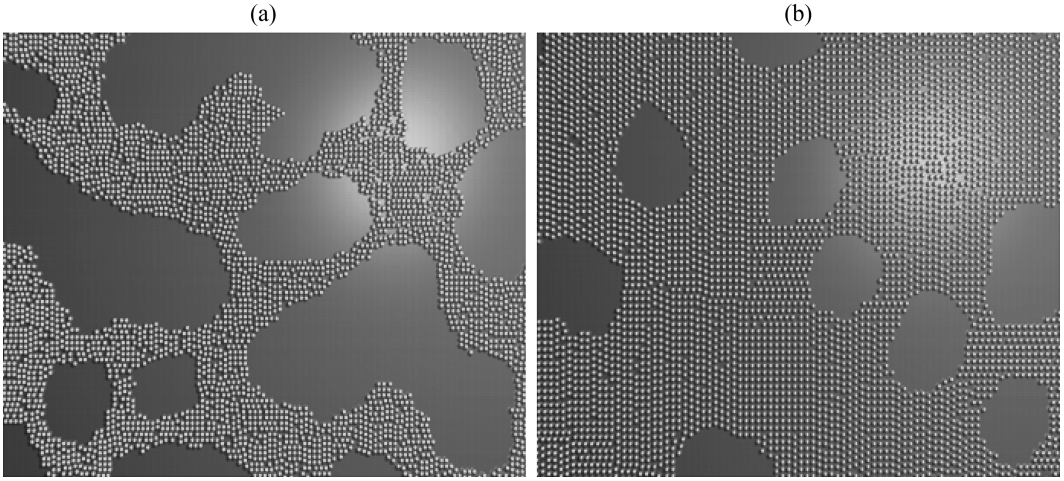

Fig. 8.18 Three-dimensional renderings of typical nanoparticle assemblies used for our charge-transport studies, simulated using the Monte Carlo model discussed in Section 8.1. (a) 40% coverage (NNET1) and (b) 80% coverage (NNET2).

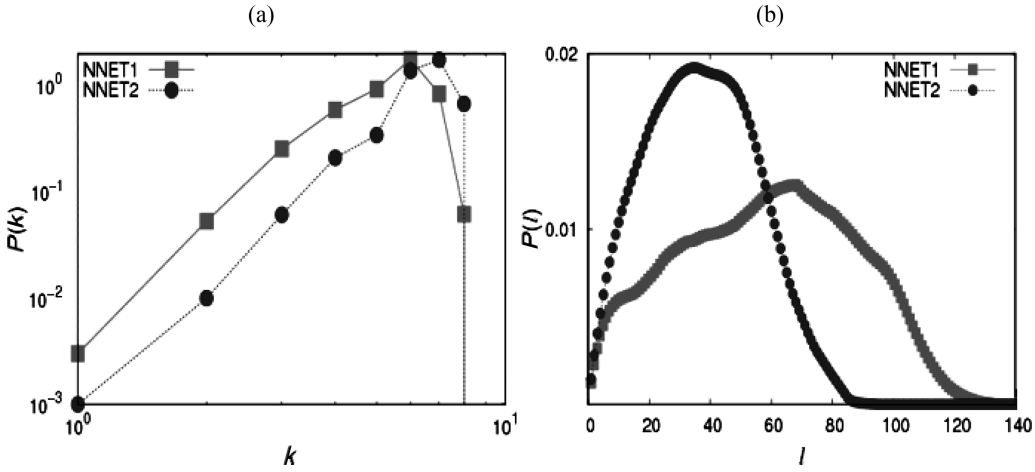

Fig. 8.19 Topological properties of two networks representing tunnelling junctions between nanoparticles in Fig. 8.18: 40% coverage (NNET1) and 80% coverage (NNET2): (a) Histograms of the number of junctions per nanoparticle and (b) Histograms of the lengths of all the shortest paths on the graph.

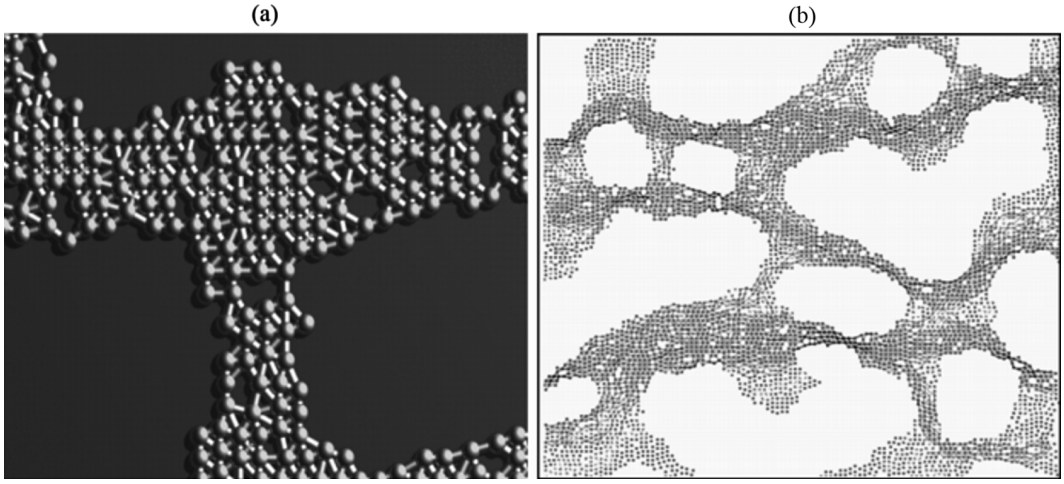

Fig. 8.20 (a) Enlarged part of nanoparticle network NNET1; (b) Simulated single-electron paths for NNET1 (Figure (b) reproduced with permission from Blunt *et al.* (2007a) ©2007 American Chemical Society).

the homogeneous film (see enlarged part of the array in Fig. 8.20(a)). Other topological features that strongly influence charge transport are the distribution of the lengths of the shortest paths and the number of such paths through each node (topological centrality). The distribution of the lengths of shortest paths between all pairs of nodes on the networks shown in Fig. 8.18 are given in Fig. 8.19(b), showing further quantitative differences between the homogeneous and inhomogeneous nanoparticle arrays.

8.3.1 Modelling single-electron conduction in nanoparticle films

As discussed above, an array of metallic nanoparticles on a substrate and under an applied voltage represents a *capacitively coupled system*, in which current transport occurs under Coulomb-blockade conditions. Following a single electron tunnelling through the junction from one nanoparticle to another, the charging energy of the nanoparticle increases inversely proportional to its capacitance. This increases the barrier for further tunnelling events through the junction. A subsequent increase of the voltage will reduce the barrier and facilitate further tunnelling processes, pushing the moving front of the electrons towards the zero-voltage electrode.

For a voltage above a certain threshold V_{T} (which depends on the sample size), the profile of the voltage across the sample is sufficient to push the front of charge to reach the opposite electrode. Thus, the current through the sample can be measured for voltages $V > V_{\mathrm{T}}$. Theoretical models of single-electron charge transport in nanoparticle arrays (Geigenmuller and Schon 1989; Bakhalov *et al.* 1991; Middleton and Wingreen 1993; Parthasarathy *et al.* 2001; Reichhardt and Olson Reichhardt 2003a, 2003b; Parthasarathy *et al.* 2004; Elteto *et al.* 2005) have mostly considered regular (or slightly disordered) 2-dimensional and 1D geometries. Recently, we generalized the model for any 2D structure formed by the Rabani *et al.* (2003) Monte Carlo approach and variants thereof (Maertin *et al.* 2004; Martin *et al.* 2007a; Pauliac-Vaujour *et al.* 2008). Each nanoparticle array generated by the Monte Carlo self-organization code can be represented by a network of junctions, as described above, and given by the network adjacency matrix $\mathbf{A}$. Note that the elements of the adjacency matrix $A_{ij} = 1$ if the particles (i, j) are within a tunnelling distance, and $A_{ij} = 0$ otherwise. Here, we will describe the main features of single-electron conduction within the generalized model. A more detailed description and the numerical implementation of the model can be found in Šuvakov, and Tadić, (2008b).

Following Geigenmuller and Schon (1989), Bakhalov *et al.* (1991), and Middleton and Wingreen (1993), the tunnelling process through arrays of nanoparticles separated by RC junctions can be described by considering the electrostatic energy of the assemble. We use the generalized expression for charge, Q_i, on the ith nanoparticle within the array, which has a given topology of connections A_{ij} (Blunt *et al.* 2007b, Šuvakov and Tadić 2008):

$$Q_i = \sum_j C_{ij}(\Phi_i - \Phi_j) + \sum_\mu C_{i,\mu}(\Phi_i - \Phi_\mu), \tag{8.13}$$

where Φ_i is the potential of the ith nanoparticle, $C_{ij} \equiv C A_{ij}$ is the capacitance between the ith and the jth nanoparticle, $C_{i,\mu}$ is the capacitance between the ith nanoparticle and electrode $\mu \in \{+, -, gate\}$, Φ_μ is the chemical potential, and Q_μ is the charge on the electrode μ. This system of equations can be written in matrix form $\mathbf{Q} = M\Phi - \mathbf{C}_\mu \Phi^\mu$ and solved for Φ:

$$\Phi = M^{-1}\mathbf{Q} + M^{-1}\mathbf{C}_\mu \Phi^\mu, \tag{8.14}$$

where M is the capacitance matrix of the whole system (nanoparticle array and electrodes):

$$M_{ij} = \delta_{i,j}\left(\sum_k C_{ik} + \sum_\mu C_{i,\mu}\right) - C_{ij}. \tag{8.15}$$

With these definitions the electrostatic energy of the entire system can be written in matrix form as (Geigenmuller and Schon 1989, Bakhalov *et al.* 1991, Middleton and Wingreen 1993, Šuvakov and Tadić 2008):

$$E = \frac{1}{2}\mathbf{Q}^\dagger M^{-1}\mathbf{Q} + \mathbf{Q}\cdot V^{\text{ext}} + Q_\mu \Phi^\mu, \quad V^{\text{ext}} = M^{-1}\mathbf{C}_\mu \Phi^\mu. \tag{8.16}$$

The system is driven by increasing the external voltage V^{ext} at one of the electrodes, which causes electrons to first tunnel to nearest-neighbor particles and then forward through the junctions between the nanoparticles. Due to the overall voltage profile, tunnelling is predominantly towards the zero-voltage electrode as $+V \to a \to b \to \ldots \to -V$. The gate voltage is kept fixed $V_{\text{g}} = 0$.

Following a single electron tunnelling from nanoparticle $a \to b$, which causes a change of the local charge as $Q_i' = Q_i + \delta_{ib} - \delta_{ia}$, the energy change $\Delta E(a \to b)$ of the array can be computed from eqn (8.16) for a given voltage V^{ext}. Introducing the variable

$$V_c \equiv \sum_i Q_i M_{ic}^{-1}; \tag{8.17}$$

one can express the energy change $\Delta E(a \to b)$ as follows

$$\Delta E(a \to b) = V_b - V_{\text{a}} + \frac{1}{2}(M_{aa}^{-1} + M_{bb}^{-1} - M_{ab}^{-1} - M_{ba}^{-1}), \tag{8.18}$$

where V_{a} and V_b are computed via eqn (8.17) and an additional contribution $V_b^{\text{ext}} - V_{\text{a}}^{\text{ext}}$ comes from the second term in expression (8.16). Note also that the energy changes due to tunnellings between the electrodes and a nanoparticle can be expressed as $\delta E(a \leftrightarrow \pm) = \pm V_{\text{a}} + \frac{1}{2}M_{aa}^{-1}$. These forms are suitable for numerical implementation, where the updated value V_c' at a node c after the tunnelling $a \to b$ can be calculated recursively according to:

$$a \to b: \quad V_c' = V_c + M_{bc}^{-1} - M_{ac}^{-1}, \quad a \leftrightarrow \pm. \quad V_c' = V_c \pm M_{ac}^{-1}. \tag{8.19}$$

All details regarding the numerical implementation are discussed in Šuvakov and Tadić (2008). We describe here the main features of the simulations that are necessary to understand the results. For a given voltage V at one electrode, the tunnelling processes are simulated as follows. At each time step, following a tunnelling event $a \to b$, the energy changes $\Delta E_{i\to j}$ at each junction $i \to j$ are calculated, including the junctions between nanoparticles and the electrodes $\pm$. The *tunnelling rate* $\Gamma_{i\to j}$ of an electron tunnelling from $i \to j$ is then determined as:

$$\Gamma_{i\to j}(V) = \frac{1}{eR_{i\to j}} \frac{\Delta E_{i\to j}/e}{1 - \mathrm{e}^{-\Delta E_{i\to j}/k_{\text{B}}T}}. \tag{8.20}$$

Here, $R_{i\to j}$ is the so-called *quantum resistance* of the junction, which appears as a parameter in the macroscopic theory. It determines the characteristic timescale of the tunnellings as $\tau \sim RC_{\rm g}$. Here, we assume $R_{i\to j} = R$ for all junctions. (For a junction between metallic nanoparticles the tunnelling resistance is obtained within the transfer Hamiltonian method as $R = \hbar/2\pi e^2|T_0|^2 D_0^2$, where T_0 and D_0 are the transmission coefficient and the density of states for each nanoparticle (Ferry and Goodnick 1997). Generally, for a junction between small nanoparticles the quantum resistance (conductance) is readily computed, for instance within density-functional theory (Reimann and Manninen 2002), exhibiting a characteristic dependence on the gate voltage and the electronic states of the dots.)

In our continuous-time implementation (Šuvakov and Tadić 2008), we determine from the tunnelling rates $\Gamma_{i\to j}$ the time t_{ij} for each tunnelling event. Then, the processes whose tunnelling times are in a given small time window are performed first, and the energy is updated at all junctions. In the limit when the capacitance of the gate $C_g >> C$, the diagonal elements of the capacitance matrix are dominant and one can reduce the number of terms to be included in the calculations (Šuvakov and Tadić 2008). The net current through a junction $i \leftrightarrow j$ is then given by

$$I_{i\leftrightarrow j}(V) = e\left(\Gamma_{i\to j}(V) - \Gamma_{j\to i}(V)\right). \tag{8.21}$$

The current through the system is measured at the zero-voltage electrode as the total current at the junctions between the last layer of nanoparticles and that electrode. In these stochastic tunnelling processes, the number of electrons through each junction is fluctuating in time. For large enough voltage above the threshold voltage $V > V_{\rm T}$ there is a finite average number of electrons arriving at the electrode at each time step, which gives a constant current $I(V)$. In the simulations we keep track of the number of tunnel events (flow) at each junction in the network. In Fig. 8.20(b) we show the conduction paths throughout the network (the electrodes are along the left and the right boundary): Darker color represents larger flow on the junction. Clearly, some junctions (and their adjacent nanoparticles) are used more often than others, depending on their position between the electrodes and the overall nanoparticle array structure. A complete statistical analysis of the flow (dynamical centrality) of junctions is given by Šuvakov and Tadić (2008).

In conducting nanoparticle arrays a non-linear current–voltage dependence of the following form was measured (Parthasarathy *et al.* 2001, Parthasarathy *et al.* 2004, Blunt *et al.* 2007a)

$$I(V) = B\left(\frac{V - V_{\rm T}}{V_{\rm T}}\right)^{\zeta}, \tag{8.22}$$

where B is a constant. The degree of non-linearity measured by the exponent ζ varies with the structure of the array that as described throughout Section 8.1, is strongly dependent on the solvent dewetting dynamics. Experimentally measured values for 2D nanoparticle arrays vary from $\zeta = 2.25$ (Pathasarathy *et al.* 2001) to $\zeta = 4.3$ (Blunt *et al.* 2007a). In Fig. 8.20(a) we show simulation results for several representative regular arrays, and, in Fig. 8.21(b), for the

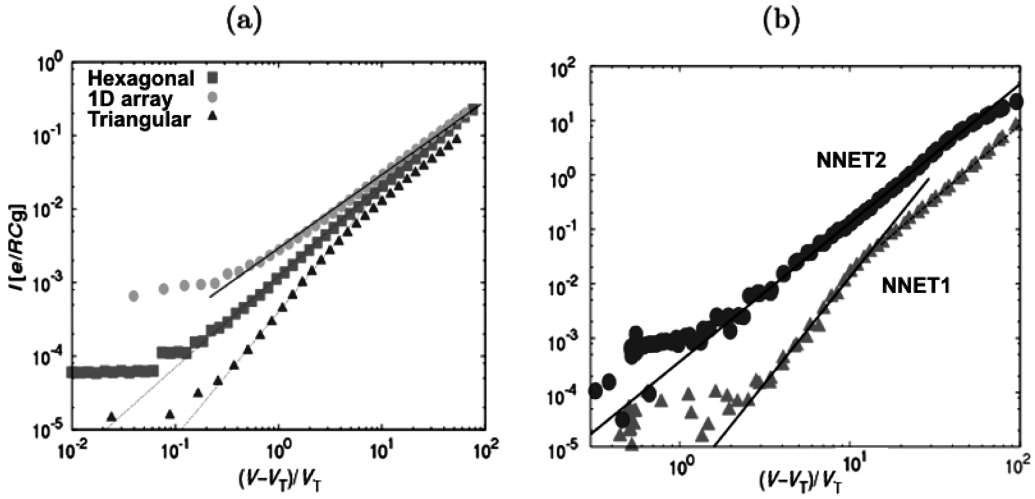

Fig. 8.21 $I(V)$ characteristics for (a) hexagonal, triangular, and 1D nanoparticle arrays in the presence of quenched charge disorder, and (b) for the topologically disordered structures shown in Fig. 8.18.

two nanoparticle arrays simulated by the Rabani *et al.* (2003) code (NNET1 and NNET2; see Figs. 8.18(a,b)). In the case of a linear chain of nanoparticles, the $I(V)$ dependence is linear, despite the stochastic nature of the tunnelling processes. This suggests that the non-linearity in eqn (8.22) is a topological effect due to multiple conducting paths in 2D arrays. Furthermore, the geometry of the shortest paths between the electrodes, which contribute to the onset of conduction at the threshold voltage, depend strongly on the topology of the nanoparticle network. These effects are combined with the next-shortest paths, etc., enhancing non-linear effects when the voltage is increased. For very large voltages the barriers for tunnelling across the junctions along the paths are too low and the $I(V)$ curve bends towards the classical linear behavior.

Non-linear current–voltage characteristics are found for a wide range of voltages above threshold, both in simulations and experiments. In a regular hexagonal array of nanoparticles, $\zeta \approx 3$ was found (Šuvakov and Tadić 2008) in the absence of charge disorder. In Fig. 8.21(a) we show the results for regular arrays in the presence of *quenched charge disorder*: at each nanoparticle the charge Q_i has a random non-integer offset q_i, taken from a uniform distribution in the range $0 \leq q_i \leq e$. The presence of the charge disorder affects the local relation between the charge Q_i of moving electrons and the voltage. This blocks the tunnelling process along some junctions, thus reducing the number of topologically available shortest paths. The total current through the sample is reduced compared with the non-disordered case for the same voltage. Consequently, we find lower values of the exponent ζ in the presence of quenched charge disorder. Again, the effects depend on the geometry of the regular array: the exponent reduction is stronger in the case of an hexagonal than in a triangular array. The exponent in the case of the linear chain of nanoparticles is not affected by charge disorder.

In contrast to the quenched charge disorder discussed above, *topological* disorder, as observed in the self-assembled nanoparticle arrays in Fig. 8.18,

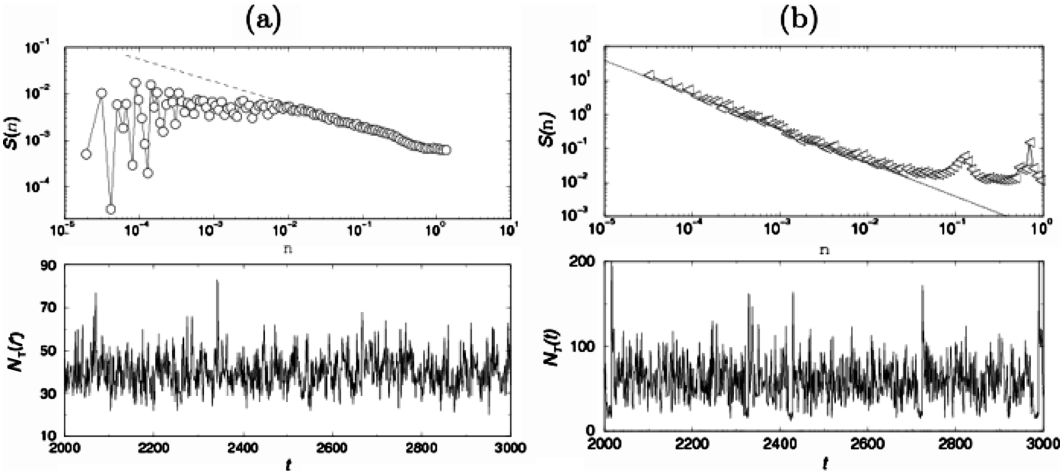

Fig. 8.22 Time series of the total number of tunnellings (bottom panels) and their power spectra (top panels) for: (a) regular triangular nanoparticle array with charge disorder and (b) Nanoparticle network NNET1 (see Fig. 8.18).

enhances the $I(V)$ non-linearity. The curves in Fig. 8.21(b) are the simulation results for the networks of Figs. 8.18(a,b). Network NNET1, with 40% coverage and large topological inhomogeneity (cf. Fig. 8.19), exhibits a larger non-linearity of the current with the exponent $\zeta \approx 3.9$. For the more homogeneous network, NNet2, $\zeta \approx 2.6$, comparable with that observed for regular arrays without charge disorder.

In stochastic tunnelling processes the charge at each nanoparticle fluctuates in time. We thus observe a fluctuating time series $\{Q_i(t)\}$, $i = 1, 2, \cdots N$ for each nanoparticle in the network. The number of tunnel events occurring at the same instance of time in the whole system, $N_T(t)$, provides an important measure of time correlation in the conduction process. $N_T(t)$ fluctuates over a well-defined average value when current flows through the array, i.e. for $V > V_T$, making a *stationary time series*. Two examples of such time series are shown in Fig. 8.22 for the regular array with charge disorder and for the topologically inhomogeneous network NNET1. The power spectra of these two time series, shown in the top panels in Fig. 8.22, appear to be entirely different. In particular, the total number of tunnel events in NNET1 exhibits long-range correlations in time with the power spectrum

$$S(\nu) \sim \nu^{-\beta}, \tag{8.23}$$

and the exponent $\beta \approx 1$ ($1/\nu$ noise) in a wide range of frequencies. On the contrary, the spectrum of the tunnellings in the regular triangular array with quenched charge disorder shows only weak correlations in the high-frequency region, and white-noise behavior for a range of low frequencies. Somewhat similar long-range correlations in the power spectra of current fluctuations have recently been measured for conducting nanowires (Kohno and Takeda 2007).

The long-range correlations in the power spectrum in the case of self-assembled nanoparticle arrays, together with other statistical properties of the conduction process (correlations between successive events at each

nanoparticle, distribution of flow along conduction paths, dispersion of the time series at each node, and current fluctuations) studied in detail by Šuvakov and Tadić (2008), reveal that the non-linearity in the current–voltage curves arises as a collective dynamical effect in these systems.

8.4 Conclusion

In this chapter we have given a brief overview of a number of key themes in state-of-the-art nanoscience: biomimetic strategies for nanoparticle self-assembly, pattern formation and self-organization in dewetting nanofluids, and charge transport in extended arrays of metal nanoparticles. Our aim has not been to present an exhaustive review of the (extensive) literature in these areas but to provide the reader with some insight into recent advances in these exciting subfields of nanoscience. There remain many challenges with regard to extending our ability to direct the organization and assembly of matter across a hierarchy of length scales (nanometers–micrometers–millimeters) but it is clear that very simple experiments, bearing much in common with work on the physics of coffee stains (Deegan *et al.* 1997), can yield remarkable and facile new methods of controlling nanoparticle organization. While the experiments are straightforward, their interpretation, modelling, and analysis are, however, far from simple. The physics of nanoparticle ensembles is a rich and complex area of modern condensed-matter science that will continue to provide key insights into the dynamics of self-assembly and self-organization in nanostructured matter.

Acknowledgments

We are grateful for the financial support of the EU Framework Programme 6 Marie Curie scheme (under grant MRTN-CT-2004005728 (PATTERNS)). We also acknowledge funding from the UK Engineering and Physical Sciences Research Council (in the form of a doctoral training account (DTA) PhD studentships). BT acknowledges program P1-0044 (Slovenia) for funding. We thank the members of the PATTERNS network for helpful discussions regarding pattern formation in nanoparticle assemblies including, in particular, Uwe Thiele, Ulli Steiner, James Sharp, and Mathias Brust. In addition, we thank Bryan Gallagher and Laurence Eaves for providing access to the cryostats used in this work, and Eran Rabani and Juan P Garrahan for very helpful discussion in relation to Monte Carlo simulations.

References

Archer, P. I., Santangelo, S. A., and Gamelin, D. R. Nano Lett. **7**, 1037 (2007).

Avouris, P., Hertel, T., and Martel, R. Appl. Phys. Lett. **71**, 285 (1997).

Bakhvalov, N., Kazacha, G., Likharev, K., and Serdyukova, S. T. Physica B **173**, 319 (1991).

Bigioni, T. P., Lin, X. M., Nguyen, T. T., Corwin, E. I., Witten, T. A., and Jaeger, H. M. Nature Materials, **5**, 265 (2006).

Blunt, M.O, Martin, C. P., Ahola-Tuomi, M., Pauliac-Vaujour, E., Sharp, P., Nativo, P., Brust, M., and Moriarty, P. J. Nature Nanotech. **2**, 167 (2007a).

Blunt, M. O., Šuvakov, M., Pulizzi, F., Martin, C. P., Pauliac-Vaujour, E., Stannard, A., Rushforth, A. W., Tadić, B., and Moriarty, P. Nano Lett. **7**, 855 (2007b).

Brennan, J. L., Hatzakis, N. S., Tshikhudo, T. R., Dirvianskyite, N., Razumas, V., Patkar, S., Vind, J., Svendsen, A., Nolte, R. J. M, Rowan, A. E., and Brust, M. Bioconjug. Chem. **17**, 1373 (2006).

Cheng, G. J., Puntes, V. F., and Guo, T. J. Colloid Interf. Sci. **293**, 430 (2006)

Collier, C. P., Vossmeyer, T. and Heath, J. R. Ann. Rev. Phys. Chem. **49**, 371 (1998).

Dagata, J. A., Schneir, J., Harary, H. H., Bennett, J., and Tseng, W. J. Vac. Sci. Technol. B **9**, 1384 (1991)

Deegan, R. D., Bakajin, O., Dupont, T. F., Huber, G., Nagel, S. R., and Witten, T. A. Nature **389**, 827 (1997).

Denkov, N. D., Velev, O. D., Kralchevsky, P. A., Ivanov, I. B., Yoshimura, H., and Nagayama, K. Langmuir **8**, 3183 (1992).

Duruöz, C. I., Clarke, R. M., Marcus, C. M. Harris, Jr., J. S. Phys. Rev. Lett. **74**, 3237 (1995).

Elteto, K., Lin, X.-M., and Jaeger, H. Phys. Rev. B **71**, 205412 (2005).

Ferry, D. K. and Goodnick, S. M. *Transport in nanostructures*, Cambridge University Press, (1997).

Ge, G. and Brus, L. J. Phys. Chem. B **104**, 9573 (2000).

Geigenmuller, U. and Schon, G. Europhys. Lett. **10**765 (1989).

Gigault, C., Dalnoki-Veress, K., and Dutcher, J. R. J. Colloid Interf. Sci. **2001**, **243**, 143 (2001).

Guéron, S., Deshmukh, M. M., Myers, E. B., and Ralph, D. C. Phys. Rev. Lett. **83**, 4148 (1999).

Huang, J., Kim, F., Tao, A. R., Connor, S., and Yang, P. Nature Mater. **4**, 896 (2005).

Huber, R. Science **233**, 702 (1986).

Jacobs, K., Herminghaus, S., and Mecke, K. R. Langmuir, **14**, 965 (1998).

Jang, J. and Oh, J. H. Langmuir **20**, 8419 (2004)

Jelesarov, I., Leder, L., and Bosshard, H. R. METHODS: A Companion to Methods in Enzymology **9**, 533 (1996) (1996).

Kardar, M., Parisi, G., and Zhang, Y.-C. Phys. Rev. Lett. **56**, 889 (1986).

Koch, S. W., Desai, R. C., and Abraham, F. F. Phys. Rev. A **27**, 2152 (1983).

Kohno, H. and Takeda, S. Nanotechnology **18**, 395706 (2007).

Korgel, B. A. and Fitzmaurice, D. Phys. Rev. Lett. **80**, 3531 (1998).

Liron, Z., Bromberg, A. and Fisher, M. *Novel approaches in biosensors and rapid diagnostic assays*, Kluwer Academic/Plenum Publishers (2001).

Lu, N., Chen, X. D., Molenda, D., Naber, A., Fuchs, H., Talapin, D. V., Weller, H., Muller, J., Lupton, J. M., Feldmann, J., Rogach, A. L., and Chi, L. F. Nano Lett. **4**, 885 (2004).

Maillard, M., Motte, L., Ngo, A. T., and Pileni, M. P. J. Phys. Chem. B **104**, 11871 (2000).

Martin, C. P., Blunt, M. O., and Moriarty, P. Nano Lett. **4**, 2389 (2004).

Martin, C. P., Blunt, M. O., Pauliac-Vaujour, E., Stannard, A., Moriarty, P., Vancea, I., and Thiele, U. Phys. Rev. Lett. **99**, 116103 (2007a).

Martin, C. P., Blunt, M. O., Vaujour, E., Fahmi, A., D'Aleo, A., De Cola, L., Vögtle, F., and Moriarty, P. "*Self-organised nanoparticle assemblies; A panoply of patterns*", in *Systems self-assembly: Interdisciplinary snapshots* ed. Krasnogor, N.; Gustafson, S.; Pelta, D.; Verdegay, J. L., (Elsevier) (2007b).

Middleton, A. and Wingreen, N. Phys. Rev. Lett. **71**, 3198 (1993).

Mirkin, C. A., Inorg. Chem. **39**, 2258 (2000).

Mirkin, C. A., Letsinger, R. L., Mucic, R. C., and Storhoff, J. J. Nature **382**, 607 (1996).

Moriarty, P., Taylor, M. D. R., and Brust, M. Phys. Rev. Lett. **89**, 248303 (2002).

Mossa, S., Sciortino, F., Tartaglia, P., and Zaccarelli, E. Langmuir **20**, 10756 (2004).

Murray, C. B., Kagan, C. R., and Bawendi, M. G. Ann. Rev. Mater. Sci. **30**, 545 (2000).

Narayanan, S., Wang, J., and Lin, X.-M. Phys. Rev. Lett. **93**, 135503 (2004).

Nykypanchuk, D., Maye, M. M., van der Lelie, D., and Gang, O. Nature **451**, 549 (2008).

Ohara, P. C., and Gelbart, W. M. Langmuir **14**, 3418 (1998).

Ohara, P. C., Heath, J. R., and Gelbart W. M. Angew. Chem. Int. Ed. **36**, 1078 (1997).

Park, S. Y., Lytton-Jean, A. K. R., Lee, B., Weigand, S., Schatz, G. C., and Mirkin, C. A. Nature **451**, 553 (2008).

Parker, A. J., Childs, P. A., Palmer, R. E., and Brust, M. Nanotechnology **12**, 6 (2001).

Parthasarathy, R., Lin, X.-M, Elteto, K., Rosenbaum, T., and Jaeger, H. Phys. Rev. Lett. **92**, 076801 (2004)

Parthasarathy, R., Lin, X.-M., and Jaeger, H. Phys. Rev. Lett. **87**, 186807 (2001) (2001).

Pauliac-Vaujour, E., and Moriarty, P. J. Phys. Chem. C **111**, 16255 (2007).

Pauliac-Vaujour, E., Stannard, A., Martin, C. P., Blunt, M. O., Moriarty, P., Vancea, I., and Thiele, U. Phys. Rev. Lett. **100**, 176102 (2008).

Pearson, J. R. A. J. Fluid. Mech., **4**, 489 (1958).

Pileni, M. P. J. Phys. Chem. B **105**, 3358 (2001).

Pileni, M. P. J. Phys.: Condens. Matter **18**, S67 (2006).

Pileni, M. P. Acc. Chem. Res. **40**, 685 (2007).

Rabani, E., Reichman, D. R., Gleissler, P. L., and Brus, L. E., Nature **426**, 271 (2003).

Reichhardt, C. and Olson Reichhardt, C. J. Phys. Rev. B **68**, 165305 (2003a).

Reichhardt, C. and Olson Reichhardt, C. J. Phys. Rev. Lett. **90**, 046802 (2003b).

Reimann, S. M. and Manninen, M. Rev. Mod. Phys., **74**, 1283 (2002).

Shafi, K. V. P. M, Felner, I., Mastai, Y., and Gedanken, A. J. Phys. Chem. B **103**, 3358 (1999).

Shen, T. C., Wang, C., Abeln, G. C., Tucker, J. R., Lyding, J. W., Avouris, Ph., and Walkup, R. E. Science, **268**, 1590 (1995).

Storhoff, J. J. and Mirkin, C. A. Chem. Rev., **99**, 1849 (1999).

Stowell, C. and Korgel, B. A. Nano Lett. **1**, 595 (2001).

Šuvakov M. and Tadić B. *Structure of colloidal aggregates with bio-recognition bonding*, unpublished (2008a).

Šuvakov, M. and Tadić, B. submitted (2008b).

Tadić, B. *From Microscopic rules to emergent cooperativity in large-scale patterns*, in "Systems Self-Assembly: Multidisciplinary Snapshots", ed. N. Krasnogor *et al.*, Elsevier (2007).

Thiele, U., Mertig, M., and Pompe W. Phys. Rev. Lett. **80**, 2869 (1998).

Thiele, U. Eur. Phys. J. E. **12**, 409 (2003).

Winfree, E., Liu, F., Wenzler, L. A., and Seeman, N. C. Nature **394**, 539 (1998).

Xu, J., Xia, J., and Lin, Z. Angew. Chem. Int. Ed. **46**, 1860 (2007).

Yosef, G. and Rabani, E. J. Phys. Chem. B **110**, 20965 (2006).

Zaccarelli, E. J. Phys.: Cond. Matter **19**, 323101 (2007).

Zhou, W. L., He, J. B., Fang, J. Y., Huynh, T. A., Kennedy, T. J., Stokes, K. L., and O'Connor, C. J. J. Appl. Phys. **93**, 7340 (2003).